



RESEARCH ARTICLE

10.1002/2014GC005444

Reconciling mantle attenuation-temperature relationships from seismology, petrology, and laboratory measurements

G. A. Abers^{1,2}, K. M. Fischer³, G. Hirth³, D. A. Wiens⁴, T. Plank², B. K. Holtzman², C. McCarthy², and E. Gazel⁵

Key Points:

- Low Q_s in subarc and back-arc mantle correlates with inferred temperatures
- Lab-based predictions of Q_s are 1.5–5X higher than arc and back-arc observations
- A strong melt effect is likely on Q in the arc and back-arc mantle

Supporting Information:

- Readme
- Supporting Information Text, Figures, and Tables
- Wedge Petrology Data Tables

Correspondence to:

G. Abers,
abers@cornell.edu

Citation:

Abers, G. A., K. M. Fischer, G. Hirth, D. A. Wiens, T. Plank, B. K. Holtzman, C. McCarthy, and E. Gazel (2014), Reconciling mantle attenuation-temperature relationships from seismology, petrology, and laboratory measurements, *Geochem. Geophys. Geosyst.*, 15, doi:10.1002/2014GC005444.

Received 3 JUN 2014

Accepted 8 AUG 2014

Accepted article online 16 AUG 2014

¹Department of Earth and Atmospheric Sciences, Cornell University, Ithaca, New York, USA, ²Lamont-Doherty Earth Observatory, Columbia University, Palisades, New York, USA, ³Department of Geological Sciences, Brown University, Providence, Rhode Island, USA, ⁴Department of Earth and Planetary Sciences, Washington University, St Louis, Missouri, USA, ⁵Department of Geosciences, Virginia Polytechnic Institute, Blacksburg, Virginia, USA

Abstract Seismic attenuation measurements provide a powerful tool for sampling mantle properties. Laboratory experiments provide calibrations at seismic frequencies and mantle temperatures for dry melt-free rocks, but require $\sim 10^2$ – 10^3 extrapolations in grain size to mantle conditions; also, the effects of water and melt are not well understood. At the same time, body wave attenuation measured from dense broadband arrays provides reliable estimates of shear wave attenuation (Q_s^{-1}), affording an opportunity for calibration. We reanalyze seismic data sets that sample arc and back-arc mantle in Central America, the Marianas, and the Lau Basin, confirming very high attenuation ($Q_s \sim 25$ – 80) at 1 Hz and depths of 50–100 km. At each of these sites, independent petrological studies constrain the temperature and water content where basaltic magmas last equilibrated with the mantle, 1300–1450°C. The Q_s measurements correlate inversely with the petrologically inferred temperatures, as expected. However, dry attenuation models predict Q_s too high by a factor of 1.5–5. Modifying models to include effects of H₂O and rheology-dependent grain size shows that the effects of water-enhanced dissipation and water-enhanced grain growth nearly cancel, so H₂O effects are modest. Therefore, high H₂O in the arc source region cannot explain the low Q_s , nor in the back arc where lavas show modest water content. Most likely, the high attenuation reflects the presence of melt, and some models of melt effects come close to reproducing observations. Overall, body wave Q_s can be reconciled with petrologic and laboratory inferences of mantle conditions if melt has a strong influence beneath arcs and back arcs.

1. Introduction

Seismic attenuation has long been used to explore the state of the Earth's interior [e.g., *Knopoff*, 1964]. Attenuation, measured as the reciprocal of a quality factor Q , clearly increases (Q decreases) with increasing temperature and probably decreases with frequency [*Anderson and Given*, 1982; *Sipkin and Jordan*, 1979]. The attenuation of shear waves, Q_s^{-1} , has a documented relationship to temperature in theory and experiments [e.g., *Cooper*, 2002; *Karato and Spetzler*, 1990]. The presence of water [*Karato*, 2003] and melt [e.g., *Hammond and Humphreys*, 2000; *Faul and Jackson*, 2007] may also increase attenuation. Grain size also has an important role [*Jackson et al.*, 2002], although it is thought that compositional effects other than volatiles are minor [*Shito et al.*, 2006; *Wiens et al.*, 2008]. Recent experiments have greatly strengthened the prediction of Q_s by incorporating mantle temperatures and seismic frequencies, in synthetic olivine aggregates [*Jackson and Faul*, 2010, hereinafter JF10], in analog materials [*McCarthy et al.*, 2011, hereinafter M11], and other polyphase samples [*Sundberg and Cooper*, 2010].

Since the experiments are done on very fine-grained materials, physical models for attenuation are required to increase confidence in the large extrapolation to mantle grain sizes. Although existing models are based on different principles (section 2), they make similar predictions at laboratory grain sizes, as a result of their origin as fits to experimental data. However, they make very different predictions at mantle conditions. For example, when the JF10 and M11 models are evaluated at common temperatures and grain sizes characteristic of the laboratory (e.g., 1000–1200°C and 5 μ m), their predictions follow similar trends, but at mantle grain sizes of 5 mm they do not (Figure 1). These comparisons are done at a 0.01 Hz frequency (100 s period) typical of surface waves, and a 1 Hz frequency typical of body waves. Even within a set of

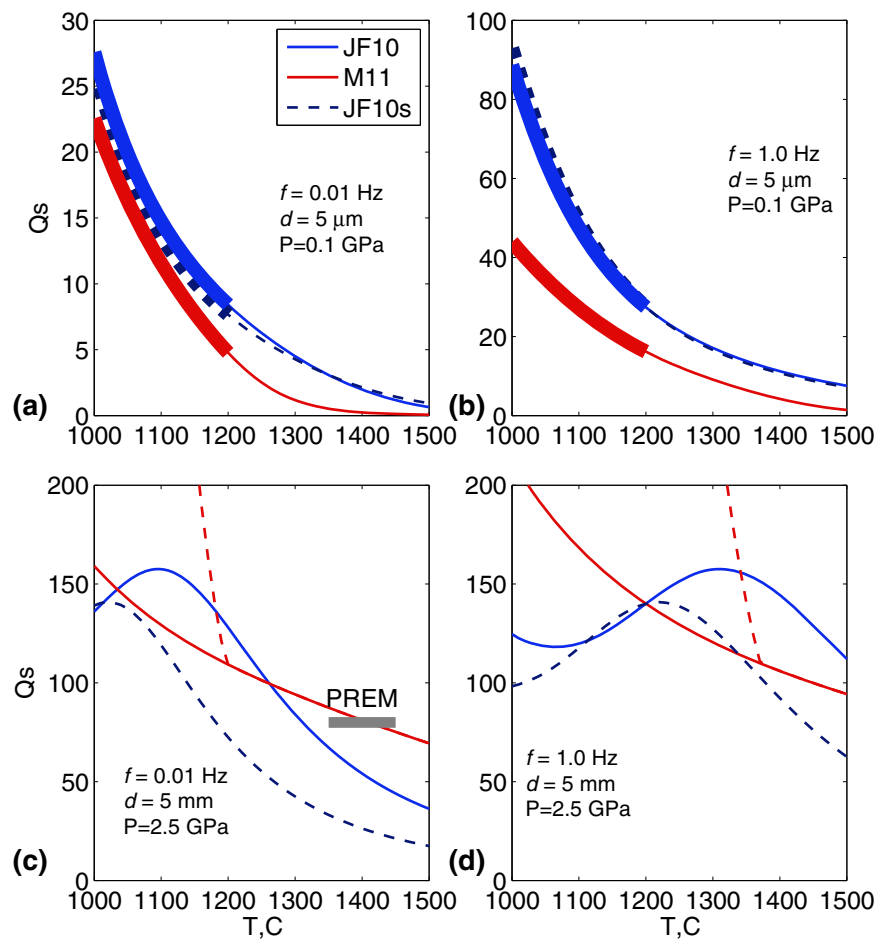


Figure 1. Shear wave attenuation predictions (Q_s^{-1}) from laboratory-based models, at laboratory ($5 \mu\text{m}$) and mantle (5 mm) grain sizes (d). Models are JF10: Jackson and Faul [2010] preferred global model; M11: McCarthy et al. [2011]; JF10s: Jackson and Faul [2010] olivine sol-gel-only fit. (a) $d = 5 \mu\text{m}$ at 0.01 Hz ; (b) $d = 5 \mu\text{m}$ at 1.0 Hz ; (c) $d = 5 \text{ mm}$ at 0.01 Hz , compared with PREM at $80\text{--}220 \text{ km}$ [Dziewonski and Anderson, 1981]; (d) $d = 5 \text{ mm}$ at 1 Hz . The frequencies span the range from surface waves (0.01 Hz) to body waves (1 Hz). Calculations are to 0.1 GPa (Figures 1a and 1b) or 2.5 GPa (Figures 1c and 1d). Thick lines in Figures 1a and 1b show range of temperatures for which olivine experimental data directly constrain Q_s , thin lines are extrapolations. Red dashed line in Figures 1c and 1d shows M11 model as originally published, solid red line shows M11 with high-frequency elastic limit extended to arbitrarily high frequency.

experiments, different assumptions result in significantly different relations; the curve labeled JF10s is the best fit of Jackson and Faul [2010] to just their small grain size sol-gel samples (i.e., excluding their coarser-grained natural olivine samples that may have slightly different properties), which results in a slightly different exponent to grain size dependence than JF10 (0.89 instead of 1.31). At 0.01 Hz surface-wave frequencies, some models can predict upper mantle attenuation models such as PREM [Dziewonski and Anderson, 1981], but in the 1 Hz body wave band little calibration exists.

At the same time, advances in seismological recording technologies and analysis methods, particularly with body waves over short paths and high resolution (spatial variation of a few tens of kilometers), have greatly increased the store of available data at frequencies of $1\text{--}10 \text{ Hz}$, providing a valuable complement to lower-frequency surface waves. Here we evaluate Q_s measurements from some recent studies in subduction zone subarc mantle and back arcs [Rychert et al., 2008; Pozgay et al., 2009; Wiens et al., 2008; Wei et al., 2013] and compare them to laboratory-derived models. In these environments, young basaltic lavas erupt on the surface and record in their major-element chemistry the pressures and temperatures at which magmas were at last in equilibrium with the mantle [Lee et al., 2009] and retain in melt inclusions undegassed water contents [Plank et al., 2013]. From these independent constraints, we observe that, while there is a correlation between Q_s^{-1} and temperature, extrapolation of the laboratory-based attenuation models predicts several times less attenuation, even when the effects of water are considered. Some other effect, probably related to melt, is needed to explain the seismic observations.

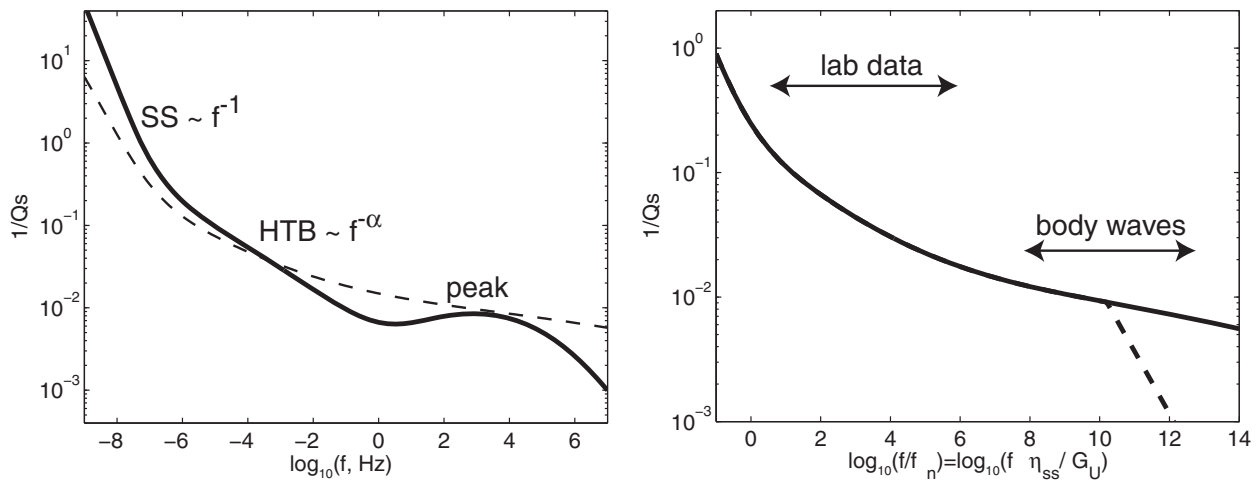


Figure 2. Attenuation models. (left) Parameterized model (JF10), solid line, showing steady state creep (SS) at low frequencies, high-temperature background (HTB) attenuation at higher frequencies, and a low-temperature, high-frequency peak. Calculated for $T = 900^\circ\text{C}$, $P = 0.2 \text{ GPa}$, and $d = 5 \mu\text{m}$. Dashed line shows M11 at same conditions. (right) Master curve (M11) for frequency normalized to f_n . Dashed line shows published high- f elastic limit, and solid curve shows extrapolation past this arbitrary limit.

2. Laboratory-Based Attenuation Models

2.1. Attenuation, Compliance, and Viscous Response

While attenuation models have been well described elsewhere [e.g., Cooper, 2002; JF10; M11, Karato and Spetzler, 1990, and references therein], we summarize them here to illustrate the potential effects of water, melt, and other parameters. Shear attenuation, as a dynamic response of a linear solid, can be treated as the phase of frequency-dependent dynamic compliance $J(\omega)$ [Nowick and Berry, 1972], the ratio of strain to driving stress. In the Laplace/Fourier domain $J(\omega)$ can be written

$$J(\omega) = J_1(\omega) + iJ_2(\omega), \quad (1)$$

where ω is angular frequency, and attenuation Q^{-1} is

$$Q^{-1}(\omega) = J_2(\omega) / J_1(\omega). \quad (2)$$

Typical models of compliance have the form

$$J(\omega) = J_U \{ 1 + F_A(\omega) - i/\omega\tau_{ss} \}, \quad (3)$$

where $J_U = 1/G_U$ is the unrelaxed shear compliance and G_U is the unrelaxed shear modulus. The first term represents the elastic response of the system, the second term represents anelastic behavior, discussed below, while the third describes steady state creep. The Maxwell relaxation time τ_{ss} associated with steady state creep is

$$\tau_{ss} = \eta_{ss} / G_U, \quad (4)$$

where η_{ss} is the steady state viscosity. At the lowest frequencies, η_{ss} dominates so $Q^{-1} \sim \omega^{-1}$ while at the highest frequencies the response is elastic and J_U dominates (Figure 2).

2.2. Anelastic Response Models

The anelastic response $F_A(\omega)$ exhibits a broad high-temperature background (HTB) component $F_H(\omega)$ and, in many experiments and theories, a high-frequency dissipation peak $F_P(\omega)$, so $F_A(\omega) = F_H(\omega) + F_P(\omega)$ [e.g., JF10; Morris and Jackson, 2009; Sundberg and Cooper, 2010; Xu et al., 2002]. The HTB component shows $Q^{-1}(\omega)$ increasing steadily with increasing temperature (T) and decreasing weakly with increasing ω , which can be modeled as [e.g., Jackson and Anderson, 1970; Berckhemer et al., 1982; Karato and Spetzler, 1990]

$$Q^{-1}(\omega) \sim [\omega \exp(E/RT)]^{-\alpha}, \quad (5)$$

where $\alpha = 0.1-0.4$ [Jackson et al., 2002; Karato and Spetzler, 1990] and R is the ideal gas constant. $F_H(\omega)$ also shows sensitivity to grain size d [Jackson et al., 2002] and water content [Aizawa et al., 2008]. Often $F_H(\omega)$ is

described by a series of linear elastic solids or Burgers elements with amplitudes $D(t)$ [e.g., *Anderson and Given, 1982*], which together give power law dependence of Q on ω :

$$F_H(\omega) = \Delta \int_{\tau_L}^{\tau_H} \frac{(1 + i\omega t)D(t)dt}{(1 + \omega^2 t^2)}, \quad (6)$$

where Δ is a scaled relaxation strength, the absorption band is defined as periods $\tau_L < t < \tau_H$, and

$$D(t) = \frac{\alpha t^{\alpha-1}}{(\tau_H^\alpha - \tau_L^\alpha)}. \quad (7)$$

Alternatively, the HTB can be represented as an Andrade rheology [*Gribb and Cooper, 1998; Sundberg and Cooper, 2010*],

$$F_H(\omega) = \beta \Gamma(1 + \alpha) (i\omega)^{-\alpha}, \quad (8)$$

where β acts similarly to Δ to scale the dissipation strength, α again describes power law decay at high frequencies, and $\Gamma()$ is the Gamma function. In olivine experiments published to date, the data can be fit equally well by either equations (6) and (7), or (8) (JF10).

Models of elastically accommodated grain-boundary sliding predict an attenuation peak $F_p(\omega)$ at high frequencies [*Raj and Ashby, 1971; Morris and Jackson, 2009*]. Several experimental data sets show indication of such a peak, sometimes attributed to melt [*Xu et al., 2002; Jackson et al., 2004*] although a variety of material processes could produce it [e.g., *Karato and Spetzler, 1990; Cooper, 2002; Sundberg and Cooper, 2010*]. The peak is centered at period τ_p , which should vary with temperature and other parameters.

Similar to most thermally activated processes, the dependence of attenuation on T , pressure (P), grain size (d), and other variables can be extrapolated from a set of reference conditions via:

$$\tau_i = \tau_{iR} \left(\frac{d}{d_R}\right)^m \exp \left[\frac{E}{R} \left(\frac{1}{T} - \frac{1}{T_R}\right) + \frac{V}{R} \left(\frac{P}{T} - \frac{P_R}{T_R}\right) \right], \quad (9)$$

where $\tau_i = \tau_L, \tau_H$, or τ_{SS} , m is the grain size exponent, E and V are activation enthalpy and volume, and the subscript "R" represents values at a reference state near experimental conditions (e.g., JF10). In this form, the preexponential term (τ_{iR}) is estimated only once at the reference state, simplifying extrapolations to other conditions. The practical equivalence between the extended Burgers description and the Andrade description of anelasticity at experimental conditions (JF10) suggests that equation (8) can be rewritten

$$F_H(\omega) = \Gamma(1 + \alpha) (i\tau_A \omega)^{-\alpha}, \quad (10)$$

where $\beta = \tau_A^{-\alpha}$ and τ_A obeys the same scaling as other τ_i . Thus, all elements of attenuation models can be scaled as equation (9), an approach we take here.

In summary, many published models exhibit several characteristics: (1) a weak quasi power law dependence on frequency (α) over a wide frequency band; (2) a possible high-frequency secondary attenuation peak at characteristic period τ_p ; and (3) relaxation times (τ_i) that scale with d, T, P , etc. in a similar manner for anelasticity as steady state creep. Note that in all parts of $J(\omega)$, the relaxation times appear in terms of the form ($\tau_i \omega$), so the scaling of relaxation times with physical variables is equivalent to scaling with period (e.g., "pseudoperiod" scaling of JF10).

The laboratory tests are conducted at mantle temperatures and seismic frequencies. Thus, the largest uncertainty in extrapolation of the laboratory data is the influence of grain size and pressure. Unfortunately, the value of the grain size exponent m remains unclear, yet critical to reach mantle conditions (Figure 1). Steady state grain-boundary diffusional creep exhibits $m = 3$ [*Hirth and Kohlstedt, 2003; Faul and Jackson, 2007*], while many attenuation experiments (summarized in JF10) indicate $m \sim 1-1.3$ for HTB behavior and some models of elastically accommodated grain-boundary sliding predict $m \sim 1$ for τ_p [e.g., *Cooper, 2002*]. Similarly, E and V are best calibrated for steady state creep, with some constraints on E for some anelastic elements, particularly, the HTB. The influence of temperature on the behavior of any high-frequency peak remains poorly constrained.

2.3. Master Curve Scaling

A different approach was taken by M11. Rather than describing each component of the compliance separately, these authors propose that a single, master curve describes the relationship between Q^{-1} (or J) and ω , if frequency is normalized appropriately to account for physical variables. They suggest a single relationship of the form

$$Q^{-1} = X(\omega/2\pi f_M), \quad (11)$$

for some single function $X()$, where f_M is the Maxwell frequency for steady state creep $G_U/\eta_{SS} = 1/\tau_{SS}$ (using the notation of the previous section). M11 fit their data to derive a functional form for $X()$, shown in Figure 2b. This scaling works remarkably well for a wide variety of material from olivine aggregates to complex organic compounds and suggests that the period scaling in equation (9) can be generalized. The scaling extends to some melt-bearing systems [McCarthy and Takei, 2011]. Hence, for a wide variety of materials, the steady state viscosity in some sense controls the attenuation response. This approach also shows that the primary extrapolation from laboratory to mantle conditions, in normalized frequency from $(\omega/2\pi f_M) = 10^{-1} - 10^4$ (lab) to $10^7 - 10^{12}$ (mantle body waves), results from extrapolation in grain size. If $m = 3$ in equation (9), then the roughly 10^3 scaling from micron to millimeter grain sizes is equivalent to a 10^9 extrapolation in ω . At face value, such scaling is difficult to reconcile with data from JF10, Jackson *et al.* [2014], and others that $m \sim 0.9 - 1.3$ in the HTB regime, hence we test both models here. In addition, it remains unclear how to account for changes in deformation mechanism in the master curve scaling, such as would arise owing to a transition from steady state diffusion creep to dislocation creep with increasing grain size. We also note that more recent experiments indicate a breakdown in Maxwell-frequency scaling at high normalized frequency (and low temperatures), although the form of that breakdown remains unclear [Takei *et al.*, 2014].

3. Measurements of Body Wave Attenuation in Subduction Zones

Body waves, from earthquakes in subducting slabs to stations above them, provide excellent signals for measuring mantle properties. Such propagation paths are relatively short, 100–500 km, and upgoing so that raypaths bend little with perturbations to velocity structure. The resulting signals appear simple with minimal coda (Figure 3). For these reasons, path-averaged measurements provide stable estimates of Q in an absolute sense with spatial resolution exceeding that of most other methods.

In this section, we describe existing attenuation tomography models from Central America [Rychert *et al.*, 2008], the Mariana subarc and back arc [Pozgay *et al.*, 2009], and similar measurements in the Lau back arc [Roth *et al.*, 1999; Wiens *et al.*, 2008; Wei *et al.*, 2013] (section 3.2), after first reviewing the underlying method of Stachnik *et al.* [2004] developed for imaging beneath central Alaska (section 3.1). Here we concentrate on Q for S waves, which allows for a more direct comparison to laboratory data. We also reanalyze path-averaged Q values for Central America and the Marianas (section 3.3) to provide a common baseline for the tomography models, and place these results in the context of a wider range of attenuation studies (section 3.4).

3.1. Attenuation Tomography Methods

Spectra for body waves depend upon both path-averaged attenuation and the earthquake source. For a path between earthquake i and station j , the measured displacement spectrum $U_{ij}(f)$ is parameterized as:

$$U_{ij}(f) = \frac{G_{ij} M_{0i} \exp\left(-t_{ij}^* f / \pi\right)}{\left(1 + (f/f_{ci})^{2n}\right)^{1/n}}, \quad (12)$$

where M_{0i} and f_{ci} describe the source via seismic moment and corner frequency, respectively, and t_{ij}^* describes the path-integrated attenuation along the raypath,

$$t_{ij}^* = \oint_{\text{raypath-}ij} \frac{ds}{V(\mathbf{r})Q(\mathbf{r})}. \quad (13)$$

Here $V(\mathbf{r})$ is the velocity at position \mathbf{r} for the measured phase (P or S), and $Q(\mathbf{r})$ is Q at \mathbf{r} . Other terms describe frequency-independent geometrical spreading (G_{ij}) and an exponent in the source model ($n = 1$ here). In Rychert *et al.* [2008] and Pozgay *et al.* [2009], all records for each earthquake (all j for each i) are simultaneously

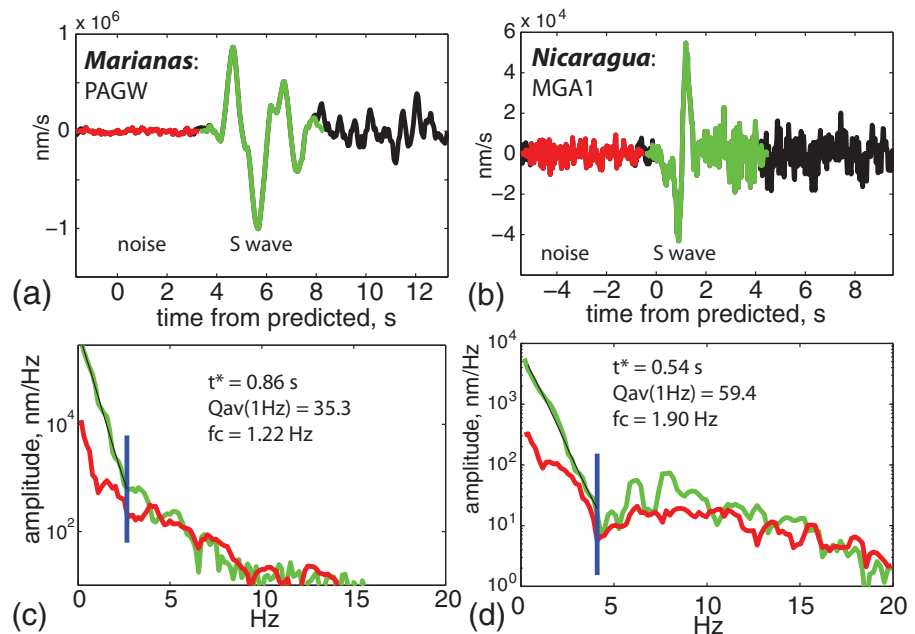


Figure 3. Examples of S wave seismograms and spectra recorded for near-identical depths and paths on two different arcs. (a and b) Transverse component S wave seismogram, raw broadband signal scaled to ground velocity. Green shows segment chosen as signal; red shows presignal noise window. (c and d) Displacement-amplitude spectrum for the signal (green) and noise (red) windows. Vertical bar shows high-frequency limit of high signal-to-noise frequency band being fit. Thin line shows best fit solution, with t^* and f_c as labeled. Stations are PAGW on Pagan volcano, Marianas, 18 km from epicenter at 126 km depth (Figures 3a and 3c), and MGA1 in Managua, Nicaragua 33 km from epicenter at 129 km depth (Figures 3b and 3d).

fit for a single set of source parameters (M_{oi} , f_{ci}) for each earthquake and separate path terms t^*_{ij} for each path. Enforcing a single source for all paths from a given earthquake reduces trade-off between corner frequency and attenuation. For strong attenuation, fall off of the displacement spectrum has a slope dominated by t^* (Figures 3c and 3d), while f_c will be constrained by less attenuating paths for the same earthquake.

A power law frequency dependence of Q such as equation (5) implies that

$$t^* = t^*_0 f^{-\alpha}. \quad (14)$$

For consistency, α is either fixed or a single value of α is solved from the complete data set. Based on typical experimental results [e.g., Karato and Spetzler, 1990; Jackson *et al.*, 2002], we fix $\alpha = 0.27$ throughout, recognizing that α varies in more complex attenuation models (e.g., JF10; M11). The reported attenuation here is based on t^*_0 , so represents attenuation projected to 1 Hz for the assumed α . Tests have shown that this approach is most sensitive to Q (or t^*) at the highest frequencies sampled [Stachnik *et al.*, 2004], which for many of the subarc and back-arc S wave data sets here is 2–5 Hz (Figures 3c and 3d), although corrected to 1 Hz via equation (14). We note that it is essential to ensure that similar assumptions about α were made, or the appropriate corrections applied, when comparing the attenuation structures from different studies.

For the Lau Basin, there is no published study using the identical analysis method, but previous work used a phase pair method incorporating spectral division between different phases to cancel the source term, and assumed frequency-independent Q [Roth *et al.*, 1999; Wiens *et al.*, 2008]. For the comparisons in this paper, we also use a Q_p structure from a new ocean bottom seismograph data set analyzed with the approach outlined in equations (12)–(14) and also assuming a frequency-dependent Q_p with $\alpha = 0.27$ [Wei *et al.*, 2013]. We convert Q_p to Q_s assuming $Q_p/Q_s = 1.7$ as obtained for the Lau back arc in prior work [Roth *et al.*, 1999], recognizing this is an added source of uncertainty.

3.2. Tomographic Models for Central America, the Marianas, and the Lau Basin

From a suite of t^*_{ij} measurements, tomographic inversion of equation (13) constrains spatial variations in Q_s^{-1} . In most cases, the small ($\ll 10\%$) uncertainties typical of $V(\mathbf{r})$ result in uncertainties in $Q(\mathbf{r})^{-1}$ that are much smaller than those due to measurement error, so the inversion can be treated as linear. Applying this

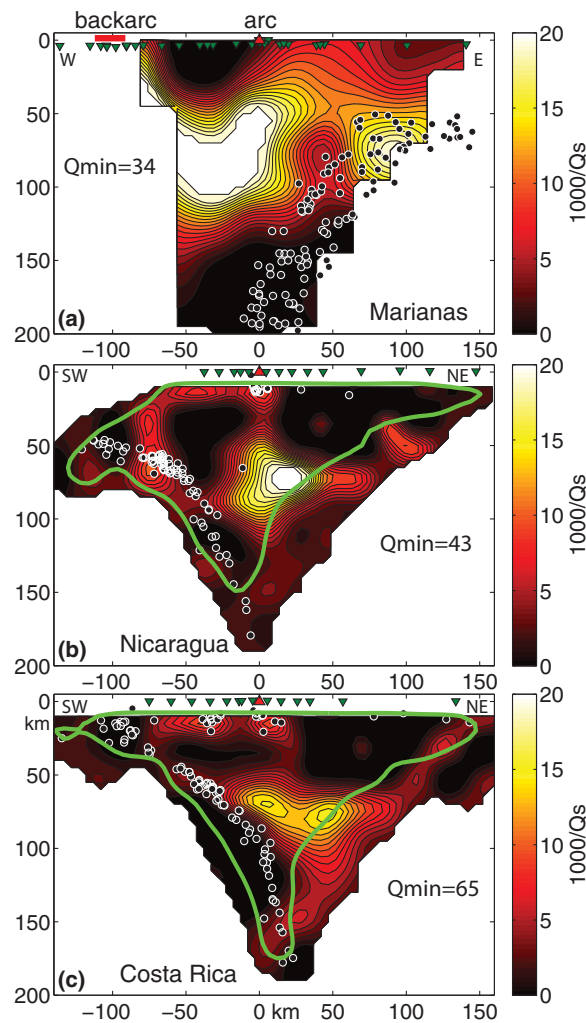


Figure 4. Results from 3-D tomographic inversions for $1000/Q_S$ from regional studies. (a) Marianas, from Pozgay *et al.* [2009]. (b) Nicaragua and (c) Costa Rica, both from Rychert *et al.* [2008]. Profile locations described in original publications. Inverted gray triangles: seismometers; red triangle: volcanic arc (Pagan, Momotombo, and Tenorio for Figures 4a–4c, respectively); circles: earthquakes located during each experiment; green line: region of high-resolution matrix diagonals. Axes show distance from arc front, km; for Figure 4a the back-arc spreading center is labeled. Minimum Q_S in each image is labeled Q_{min} .

To constrain attenuation in the melting region, we estimate the lowest Q_S imaged beneath each arc, and for the Mariana back arc. For Lau, Q_S is estimated from lower-resolution Q_P constraints [Wei *et al.*, 2013] assuming a Q_P/Q_S of 1.7 [Roth *et al.*, 1999]. Beneath arcs the minimum Q_S occurs at 70–80 km depth and within ~ 50 km horizontally from the arc, although resolution degrades farther into the back arc, so the minimum may be broader horizontally (Table 1). Uncertainties in minimum Q_S are derived for Nicaragua and Costa Rica by measuring the range of minimum Q_S values for either region from tomographic models with acceptable damping parameters [Rychert *et al.*, 2008]. For the Mariana and Lau data sets, we assume the proportional uncertainty in Q_S is the same as that in Nicaragua, where minimum Q_S is closer to Mariana and Lau values.

3.3. Path-Averaged Q_S From Central America and the Marianas

Results of tomographic studies in different regions can be difficult to compare, as different smoothing and damping parameters, as well as different ray densities can bias results. To verify that an interarc comparison of the Q_S minima obtained from the tomographic images is justified, we remeasure t^* from a subset of the

approach in two and three-dimensional inversions from the Marianas [Pozgay *et al.*, 2009] and Central America [Rychert *et al.*, 2008] shows order-of-magnitude variations in Q_S^{-1} over short distances (Figure 4). Resolution in both inversions is limited by the 20–25 km node spacing and in many areas is probably larger, as discussed in the original papers.

All images show features characteristic of subduction zones, such as high attenuation (parameterized as $1000/Q_S$) beneath and behind the arc, and low attenuation in the slab and the shallow mantle fore arc (Figure 4). Central America images illustrate the factor of 10–50 variations in $1000/Q_S$ between the subarc mantle and the cold fore-arc nose over length scales of only 20–50 km. All three also demonstrate an unfortunate feature of subduction zone attenuation measurements—the S waves on paths with the greatest cumulative dissipation are almost completely attenuated, so the highest attenuation cannot be imaged. These paths are typically from the deepest earthquakes to the stations in the back arc, for which formal resolution is also poor because crossing rays that far from the source region are absent. As a result, attenuation appears to diminish into the back arc, but it is difficult to tell from these images alone whether that is a resolution artifact. This is particularly problematic for systems having an active back-arc spreading center such as Mariana and Tonga, because the back-arc attenuation can be underestimated in the $1/Q_S$ images. In those cases, $1/Q_P$ can be used as a constraint although an assumption about the ratio Q_P/Q_S must be made.

Table 1. Minimum Q_5 Beneath Arcs and Back Arcs, 1 Hz

Arc	Minimum Q_5 Range	Source	Inferred Mantle Temperatures ($^{\circ}\text{C}$) ^a
<i>From Tomography (Figure 4)</i>			
Costa Rica	62–84	<i>Rychert et al.</i> [2008]	1304 \pm 22
Nicaragua	38–73	<i>Rychert et al.</i> [2008]	1337 \pm 35
Mariana ^b	37–71	<i>Pozgay et al.</i> [2009]	1308 \pm 21
Mariana back arc ^b	29–55	<i>Pozgay et al.</i> [2009]	1308 \pm 22
Lau back arc ^{b,c}	23–43	<i>Wei et al.</i> [2013]	1398 \pm 30
<i>Recalculated Path Averages Beneath Arc Volcanoes (Figure 5)</i>			
Nicaragua	65 \pm 10	This study	
Mariana	42 \pm 7	This study	

^aExtrapolated from magma equilibration depth to 2.5 GPa for arcs or 1.7 GPa for back arcs; uncertainty is one standard deviation of the values for individual volcanoes (for arcs) or samples (for back arcs).

^bUncertainties scaled to those for Central America.

^cScaled from Q_p ; assumes $Q_p/Q_5 = 1.7$.

verse component signals (Figure 3). These spectra are fit for source parameters and t^*_5 , inverting equation (12), assuming frequency dependence with $\alpha = 0.27$ (equation (14)). In this test, estimates of t^* , f_c , and M_0 are obtained separately for each seismogram so may suffer from f_c - t^* trade-offs more than in the original studies, but those should be relatively minor for these paths where extreme attenuation dominates spectral falloff. Because attenuation is high for these arc and back-arc paths, measurements are band-limited between 0.25 and 0.5 Hz (the lowest frequencies with detectable energy) and between 2 and 5 Hz, as illustrated in Figure 3.

These measurements are made for earthquakes 100–250 km deep and less than 50 km distant from arc volcano summits central to each array, Pagan, Momotombo, or Tenorio for the Marianas, Nicaragua, and Costa Rica, respectively. For the Central America arc, we were able to examine 5–10 signals per station for all stations, but are only able to do so in the Marianas for the land-based arc stations due to the short recording duration of many ocean bottom seismographs (OBSs) [Pozgay et al., 2009]. Also, far into the back arc it was difficult to observe S arrivals over a sufficient frequency range due to high attenuation, which meant few rays passed beneath the Mariana back-arc spreading center at great depth. The better resolved Q_p images were used as a check, assuming constant scaling between P and S . Path-averaged Q_5^{-1} is estimated by dividing the 1 Hz t^* estimates (t^*_0 from equation (14)) by total travel time as measured from seismograms. Raypaths and these measurements, along with the path-averaged Q_5^{-1} derived from the original t^*_0 measurements [Rychert et al., 2008; Pozgay et al., 2009] are shown in Figure 5.

The path-averaged Q_5 estimates generally confirm the Q_5 minima estimated from tomography (Table 1) and demonstrate that Q_5 can be compared between arcs in an absolute sense. The dense data set from Nicaragua has 140 path-averaged measurements and shows measurement consistency clearly (Figure 5b). Q_5 decreases (attenuation increases) from fore arc to back arc reaching low values of 50–100 everywhere >10 km behind the arc front, remaining relatively constant throughout the back arc. This result indicates that the apparent increase in mantle Q_5 with increasing distance into the Nicaragua back arc indicated by tomography (Figure 4b) may be a resolution artifact; Q_5 seems constant throughout the back-arc region. Measurements beneath Costa Rica are noisier and fewer, probably due to thick sediments beneath back-arc stations, but generally confirm tomographically derived values. For the stations on Pagan Island in the Mariana arc, the path-averaged Q_5 of 42 \pm 7 is at the low end of the range inferred from tomography (37–71). These relatively low path-averaged Q_5 values likely reflect a combination of the low Q_5 expected in the volcanic arc crust with Q_5 from the mantle portion of the path. The back-arc stations show path-average Q_5 of 70–110 for the Marianas, a bit higher than inferred for mantle wedge beneath the back-arc spreading center, but all of these OBSs were located on the arc side or at the spreading center so the raypaths did not sample the mantle directly beneath the spreading center.

3.4. Q Measurements From Other Regions

Similar methods have been used to estimate body wave attenuation in the mantle wedge of several subduction zones elsewhere. In northern Honshu, Nakajima et al. [2013] assumed the same frequency dependence as this study, $\alpha = 0.27$, to estimate $Q_p(1 \text{ Hz})$, and so these results are comparable to ours although a

original seismograms from which the images were obtained. Doing so allows us to apply the identical measurement approach to data from Costa Rica, Nicaragua, and the Marianas. These tests assess the extent to which Q_5 can be quantitatively compared between studies and identify any bias in anomaly amplitudes due to regularization. We repeat the measurements of t^* for S waves following Stachnik et al. [2004], for S wave displacement multitaper spectra calculated in a 3–5 s window that includes all the major energy observed on trans-

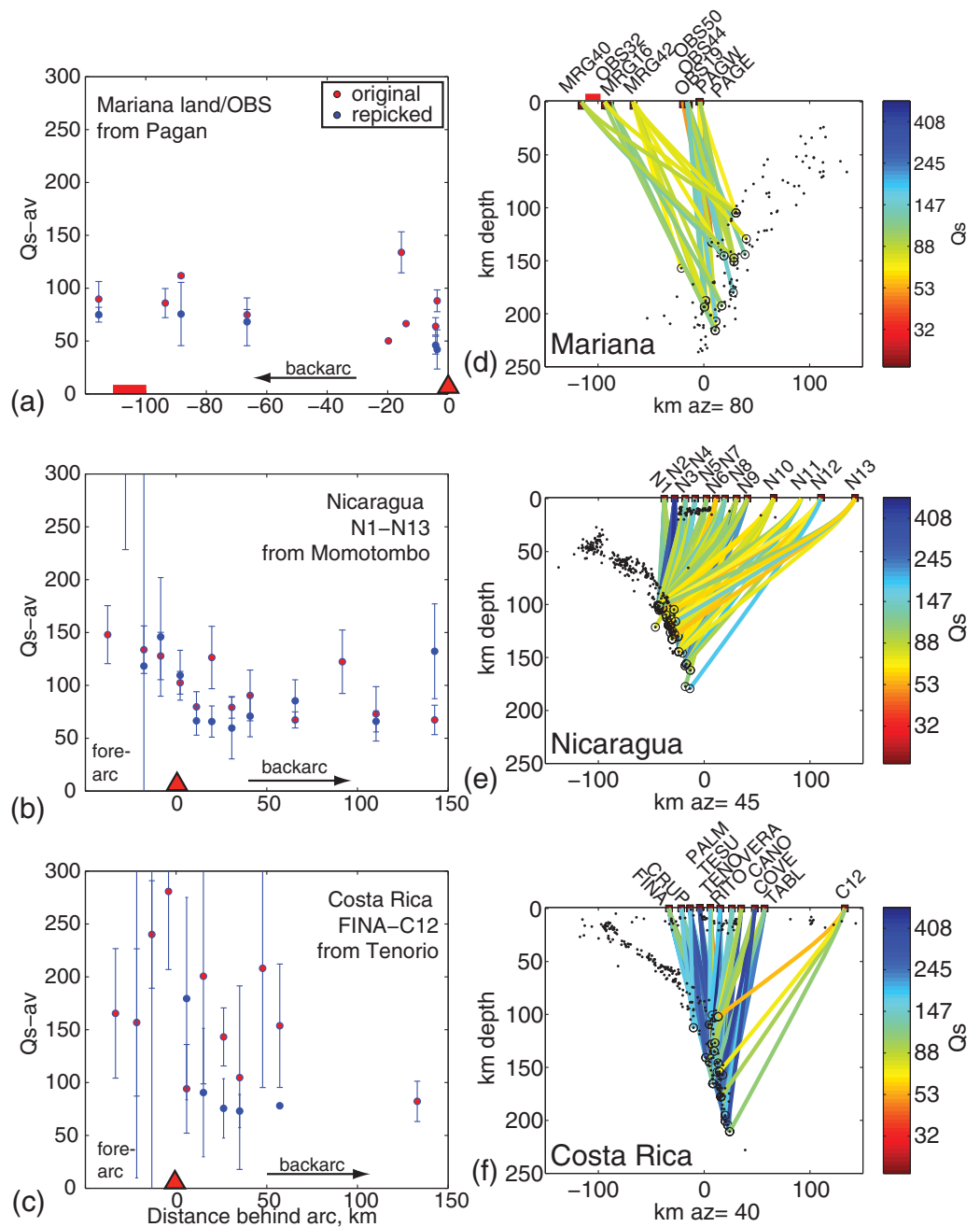


Figure 5. Path-averaged Q_s estimates from earthquakes 100–250 km deep recorded at overlying stations. (a–c) Median path-averaged Q_s for each station from data sets used in original studies [Pozgay *et al.*, 2009; Rychert *et al.*, 2008] and remeasured as described in text, varying with distance behind arc front. Error bars show median absolute deviation around each measurement, after outlier removal. (d–f) Cross sections showing earthquakes and raypaths sampled, color coded by Q_s as shown. Figures 5a and 5d for Marianas, Figures 5b and 5e for Nicaragua, Figures 5c 5f for Costa Rica. Red triangle shows arc front; red bar shows back-arc spreading center.

different source removal procedure was used. They observe a mantle wedge with $Q_p < 200$ at 65–90 km depth with a minimum of 90 ± 15 at 90 km depth, equivalent to $Q_s = 35\text{--}65$ for $Q_p/Q_s = 1.7\text{--}2.25$. These values fall in the range defined by the mantle wedges in Central America, the Marianas, and the Lau Basin. In Central Alaska, Stachnik *et al.* [2004] used the same methods and inversions as discussed here and $\alpha = 0.27$ and found a minimum Q_s of 110 ± 6 (or 95–140 from tomography) at 75 km depth. This Q_s is higher than the Central America/Marianas/Lau values, but the Alaska subduction zone segment lacks arc volcanism for 350 km along strike so perhaps melt is much less abundant or exists in less attenuative grain-scale topologies.

Other studies are more difficult to compare because of differences in methodology or assumptions, but show similar attenuation in the volcanic arcs. In the Central Andes 21°S–24°S, *Schurr et al.* [2003] measured frequency-independent Q_p and found the lowest mantle Q_p of 80–90 near 85 km depth directly beneath the arc. The most attenuating signals appear to have energy only at 7 Hz or less, suggesting minimum Q_p (1 Hz) of 50 ± 3 correcting for frequency dependence to $\alpha = 0.27$ following the correction method of *Stachnik et al.* [2004]. Immediately to the south, *Liang et al.* [2014] inverted for Q_p and Q_s and saw low Q_s in the back-arc mantle, but they allowed complicated trade-offs with α in their inversion that make comparisons difficult. *Eberhart-Phillips et al.* [2008] inverted for Q_p under North Island New Zealand with a different assumed functional dependence of Q on f , again hindering direct comparison. Nonetheless, they observe minimum Q_p (10 Hz) < 250 at 50–125 km depth beneath the volcanic line, with a minimum of 88, consistent with observations in Table 1 once Q_p/Q_s and frequency dependence are accounted for. Overall, there is ample evidence for high attenuation beneath and behind arcs at 50–90 km depths, with Q_s in the range observed here (30–75) at 1 Hz. Thus, the subarc attenuation values in Table 1 appear to be a robust feature of subduction zone mantle wedges.

At much lower frequencies, the surface-wave tomography of *Dalton et al.* [2008] yields a minimum Q_s of 60 in the 100–250 km depth range for average Pacific mantle older than 100 Ma. This Q_s minimum occurs at a depth of 160 km, dominated by waves of a period of ~ 114 s ($f \sim 0.0088$ Hz) [*Dalton et al.*, 2009]. Two factors complicate comparison of this measurement with the body wave measurements here. One is the roughly 2 orders of magnitude difference in frequency. Although some frequency dependence in Q must exist, its form at low frequencies (< 0.1 Hz) remains somewhat unclear in many regions of the Earth [e.g., *Lekic et al.*, 2009]. Second, asthenospheric mantle beneath old oceans may produce attenuation by different mechanisms than beneath arcs and back arcs, since volcanism is absent and the existence of melt is debatable. Nevertheless, these data provide a useful reference point for evaluating attenuation-viscosity relationships.

Booth et al. [2014] examine regional P waves recorded on the western Pacific seafloor from Mariana slab earthquakes, with spectral fitting and source correction methods analogous to those applied here. However, the *Booth et al.* [2014] paths are longer than in the arc/back-arc regions discussed above, and their Q estimates involve nonlinear corrections to triplicated arrivals in the transition zone. These corrections and parameterization result in large adjustments of Q_p from path-average values near 400 to inferred asthenospheric minimum values of 128–165 at 100–250 km depth, beneath a very low attenuation lithospheric layer assumed to be 100 km thick. Also, direct comparison with our subduction zone results depends again upon conversions from Q_p to Q_s . In the Lau Basin, we assumed a Q_p/Q_s of 1.7 based on *Roth et al.* [1999]. This Q_p/Q_s suggests the presence of bulk attenuation (possibly due to melt), a source of attenuation that could be absent in the suboceanic asthenosphere sampled in *Booth et al.* [2014]. Taken at face value, the *Booth et al.* [2014] results imply a Q_s of 57–73 at 1 Hz, assuming Q_p/Q_s of 2.25, or 75–97 for a Q_p/Q_s of 1.7. Owing to the pressure dependence of attenuation, this Q_s range would decrease an additional $\sim 30\%$ if it was extrapolated to the 50–80 km depth ranges where our subduction zone Q_s values are constrained (Table 1). Given these assumptions, the *Booth et al.* [2014] Q_s estimates for old oceanic mantle fall within the range of minimum subduction zone attenuation we infer for Central America, the Marianas, and the Lau Basin.

Intriguingly, the *Booth et al.* [2014] and *Dalton et al.* [2009] Q_s estimates for old Pacific mantle are also similar, despite their very different frequency bands. Either *Booth et al.* [2014] sample a region whose upper mantle differs from the broader region included in the *Dalton et al.* [2009] average for the old (> 100 Ma) Pacific, frequency dependence of Q_s is considerably less than implied by $\alpha = 0.27$ between frequencies of 0.01 and 1.0 Hz, or the apparent Q values in these studies cannot be compared due to methodological issues.

4. Petrologic Constraints

The magmas that erupt at volcanic arcs and back-arcs record in their chemical compositions the pressures, temperatures, and water contents of their mantle sources. We attempt to extract such information from the arc systems for which we have the highest resolution Q measurements, in order to investigate the influence of T and H_2O on Q .

The water concentration of mantle olivine should relate directly to equilibrium melt composition via the partition coefficient ($C_{ol} = C_{liq} * D$). Most estimates of $D_{H_2O}(ol/liq)$ are in the range of 0.001–0.002 at a pressure of ~ 1 GPa [*Hauri et al.*, 2006; *Hirschmann et al.*, 2009]. In general, volcanic arcs exhibit a remarkably

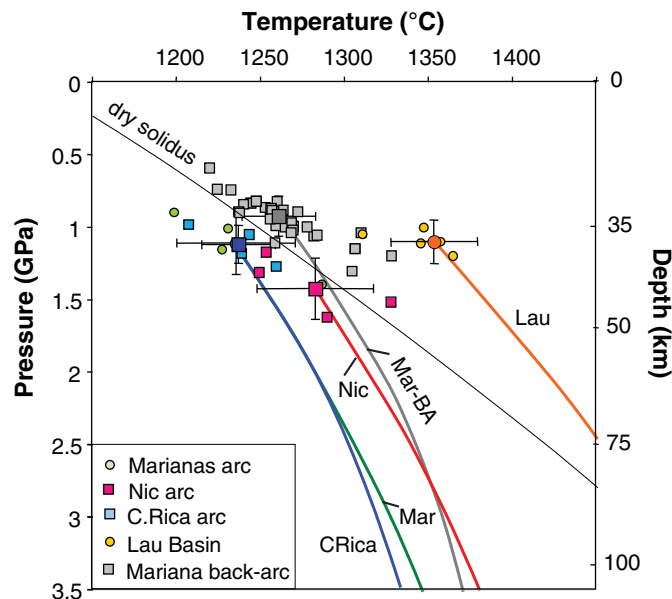


Figure 6. Pressures and temperatures of equilibration of erupted lavas with Fo_{90} mantle, calculated for most primitive melts (crystallizing olivine only) using major elements, H_2O measurements, f_{O_2} constraints, and the thermobarometer of Lee *et al.* [2009]. Average for each arc and back-arc region are shown with larger symbols and error bars for ± 1 SD. Most arc magmas last equilibrate near the top of the mantle wedge. In order to estimate temperatures in the central wedge, arc and back-arc averages are backtracked along wet melting paths, using a cryoscopic approach (modified from Gazel *et al.* [2012]; see supporting information for melting parameters and data sources). Dry solidus from Hirschmann [2000].

three arcs, respectively, given a partition coefficient of 0.0015. We thus carry out most calculations below, assuming 50 wt ppm H_2O in mantle olivine beneath the Marianas and Central American arcs. The lower water contents in Mariana back arc (1.3 wt % on average) and the Central Lau Spreading Center (0.13 wt % on average) lead to mantle olivine with 20 and 2 wt ppm H_2O , respectively.

Estimating the temperature of the mantle from magma compositions has a long tradition in olivine-melt thermometry [e.g., Roeder and Emslie, 1970; Langmuir and Hanson, 1981], which is reflected in the FeO and MgO concentrations of magma in equilibrium with mantle olivine. We use a recent calibration of the MgO ol-liq thermometer [Lee *et al.*, 2009], which is cosolved with the SiO_2 activity barometer, incorporating H_2O and f_{O_2} (oxygen fugacity) as variables. First, magma compositions are screened from data sets for the arcs and back arcs of interest, selecting only those samples that experienced the least amount of crystal fractionation, and appear to have crystallized only olivine. For the Marianas arc, for example, this reduces 215 published analyses of volcanic rocks from Pagan, Guguan, Agrigan, and Alamagan islands (within the footprint of the seismic imaging), to only 27 samples. Next, we add equilibrium olivine incrementally to these most primitive compositions (taking into account measured or estimated Fe^{3+}/Fe^{Total}) until they are in equilibrium with mantle olivine, here assumed to be Fo_{90} (Fo is the forsterite content; 1 Fo unit is the equivalent of $\sim 40^\circ C$ in the calculation). The details of the data screening and data sources are given in the supporting information.

Results based on these Fo_{90} compositions yield mantle temperatures from $1235^\circ C$ (Marianas and Costa Rica arcs) to $1385^\circ C$ (Lau Basin), at pressures uniformly lower than 1.5 GPa (~ 45 – 50 km depth; Figure 6). These temperatures reflect shallow equilibration in the mantle wedge, very near the Moho for the case of Costa Rica, and/or polybaric mixing with high volume low-pressure melts (for the back arc basins). This result is not unique to this approach; experimental phase equilibria studies on arc magmas also reflect shallow melt equilibration beneath arcs [Tatsumi *et al.*, 1983; Elkins-Tanton *et al.*, 2001]. The challenge is to extrapolate these temperatures to the depths where Q is at a minimum (75–80 km depth, or 2.5 GPa beneath the arcs, and 55 km, or 1.7 GPa beneath the back arcs). The back-arc extrapolations (from ~ 30 to 55 km) are less extreme, and can be taken along wet decompression melting adiabats (see supporting information for details). Potential temperature estimates calculated from this approach for the Marianas and Central Lau back-arc basin mantle are 1350 and $1500^\circ C$, respectively. These results are nearly identical to those

narrow range in the H_2O concentration of their most mafic melts, 3.9 ± 0.4 wt % H_2O (maximum preeruptive concentrations recorded in melt inclusions [Plank *et al.*, 2013]). The Central American and Marianas arcs are no exception; the mean is 3.4 ± 0.3 (1 SD), 4.0 ± 1.4 , and 4.5 ± 0.8 wt % H_2O , for the Costa Rica, Nicaragua, and Marianas arcs, respectively (see supporting information for data sources). Although it is possible that these H_2O concentrations are set in the crust (in which case these values are minima [Gaetani *et al.*, 2012; Plank *et al.*, 2013]), we assume that these concentrations are representative of parental melts from the mantle. If this is case, then mantle olivine in equilibrium with these melts would contain 50 ± 4 , 60 ± 20 , and 67 ± 12 wt ppm H_2O , for the same

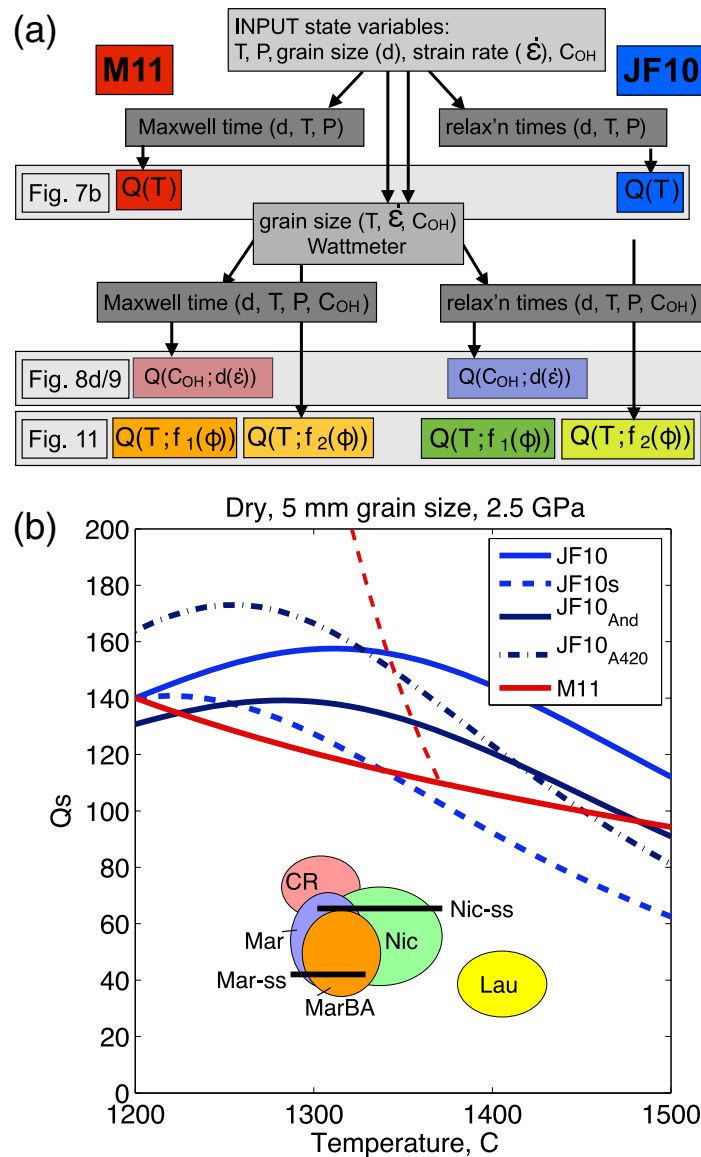


Figure 7. Comparison of body wave Q_5 and petrologically derived temperature estimates with laboratory models. (a) Flowchart of model comparisons made in this paper for laboratory-derived models JF10 and M11, showing implementation of effects of water (C_{OH}), grain size (d), melt fraction (ϕ), and other variables. (b) Comparison of data to dry constant-grain size models. Data from Table 1 are minimum Q_5 from tomography (ovals) and arc-station path averages (thick horizontal bars), at 1 Hz. Petrologically derived temperature estimates from major elements are corrected to depth of minimum Q_5 anomaly (Figure 6). Back-arc temperatures and Q_5 are extrapolated along an adiabat from 55 to 80 km depth for comparison with arc values, as described in text. Labels are CR: Costa Rica; Nic: Nicaragua; Mar: Mariana arc; Mar-BA: Mariana back arc; Lau: Lau back arc (corrected from Q_p ; see text); Mar-ss and Nic-ss, single-station path-averaged Q_5 from Pagan and Managua, respectively. Models labeled in legend: JF10, as published; JF10s, sol-gel-only extended-Burgers fit of JF10; JF10_{And}, JF10's Andrade model with low-temperature peak; JF10_{A420}, JF10_{And} but for activation energy increased from 360 to 420 kJ/mol [Behn et al., 2009]; M11, dashed as published, solid with high-frequency elastic limit removed. All calculations are done at $P = 2.5$ GPa (80 km depth), $f = 1$ Hz, and $d = 5$ mm.

presented in *Wiens et al.* [2006], based on a different approach (Fe_8 and Na_8 [Langmuir et al., 1992]) and using only dry magmas. In *Wiens et al.* [2006], the northern Lau Basin was estimated to have a potential temperature of 1450°C; our new calculations using the methods described here also predict a potential temperature of 1450°C for the northern Lau Basin. Calculations for the Central Lau Spreading Center yield higher temperatures, perhaps because of its distance from the subducting plate.

The volcanic arc results require greater extrapolation, and at the same time, there is greater uncertainty in the melting process and thermal structure. For consistency, we apply the same wet decompression melting model to the arcs. The potential temperatures calculated this way agree broadly with the back arc ones for the Marianas (1370°C for the arc versus 1350°C for the back arc). The most conservative calculation that might be done is to take the temperatures as calculated, and backtrack along a liquid adiabat (~30°C/GPa). Such temperatures (1280–1315°C at 2.5 GPa or 80 km) are within 30° of those extrapolated along wet melting paths (1310–1340°C).

5. Discussion

5.1. Comparison With Dry, Melt-Free Models

In Figure 7b, we plot our estimates for Q_5 and T (based on

major-element geochemistry) directly under arcs or back arcs where magmas are generated. The Q_5 estimates are all made from body wave spectra near 1 Hz, corrected to 1 Hz assuming $\alpha = 0.27$, plotting the minimum Q_5 from tomography or single-station path averages. Beneath arcs, Q_5 is 40–80 reaching this minimum around 80 km depth. Beneath back arcs the minimum Q_5 of 20–50 is reached at 50–60 km depth. To

compare these values directly, Q_5 for back arcs is increased slightly to its presumed equivalent value at 80 km depth, assuming pressure dependence ($V = 1.2 \times 10^5 \text{ m}^3 \text{ mol}^{-1}$) of JF10 and an adiabatic temperature gradient (0.3 K km^{-1}). With or without these corrections, we observe the highest Q_5 beneath Costa Rica and the lowest beneath the Lau back arc. These values correlate inversely with temperature estimates, which vary from near 1300°C beneath Costa Rica to greater than 1400°C beneath Lau (Table 1). The correlation supports the notion that higher temperatures lead to greater attenuation (lower Q_5), as usually presumed [e.g., Karato, 1993].

The Q_5 predictions from JF10 and M11 for a dry, melt-free olivine aggregate are calculated at 1 Hz and 2.5 GPa pressure, and a grain size of 5 mm for the mantle. The JF10 models include both their favored extended-Burgers fit and the Andrade-model fit (JF10_{And}) including the reported high-frequency absorption peak; these two models are similar, but scale slightly differently. As sensitivity tests, we also modify the Andrade fit with activation energies increased from 360 to 420 kJ/mol (JF10_{A420}), consistent with earlier estimates [Behn *et al.*, 2009], and the extended-Burgers fit of JF10 to the subset of data that includes only sol-gel samples (JF10s). As noted in section 1, the JF10s model has a modestly lower grain size sensitivity than JF10. The M11 predictions include both their published model, which includes an arbitrarily set high-frequency elastic limit, and a prediction with that limit removed to frequencies above the observation band. The latter is used in the remainder of this paper.

The laboratory-based models generally predict an inverse correlation between Q_5 and temperature, although the JF10 models show the opposite trend at temperatures $<1250\text{--}1350^\circ\text{C}$. That reversal reflects the high-frequency absorption peak indicated by the lowest temperature data in JF10; the magnitude of the peak and its scaling with grain size are not well established by these data [Jackson *et al.*, 2014], and Takei *et al.* [2014] find little evidence for it in their data. Overall, the predicted Q_5 values are all a factor of 1.5–5 higher than observed for arcs and back arcs. The discrepancy varies between models, but clearly some other factors must be accounted for to successfully predict $Q_5 < 100$ at 1 Hz and mantle wedge conditions. We test a series of effects as outlined in Figure 7a.

5.2. Grain Size

Both attenuation models JF10 and M11 exhibit large grain size dependence (Figure 1). Grain size is not an independent parameter, but a consequence of competing effects of dynamic recrystallization and grain growth. For our analyses, we use the grain size evolution model of Austin and Evans [2007] termed the paleowattmeter, as calibrated to mantle flow laws [Behn *et al.*, 2009], which predict grain size as a function of strain rate, temperature, pressure, and water content. Behn *et al.* [2009] calibrated this model using experimental data derived over a wide range of temperature and stresses. Here we demonstrate that the grain size model also provides an excellent fit to olivine grain sizes from xenoliths and exhumed section of subarc mantle.

The grain size predicted by the paleowattmeter depends on the stress and strain rate conditions, as well as the relative contributions of dislocation creep and diffusion creep to the total strain rate. For these calculations we use the flow laws for these processes determined by Hirth and Kohlstedt [2003], with C_{OH} effects recalibrated by a factor of three [Bell *et al.*, 2003]. In Figure 8a, we show the dislocation creep and diffusion creep viscosity predicted by these flow laws for a pressure of 2.5 GPa and a constant olivine water content of $C_{OH} = 50 \text{ wt ppm}$ (800 ppm H/Si), based on the arc geochemistry and water contents described in section 4; incorporating the range of observed water contents (30–70 wt ppm) produces nearly identical results. Because dislocation creep viscosities depend strongly upon strain rate, we consider a range of strain rates from 10^{-14} to $2 \times 10^{-13} \text{ s}^{-1}$ with sensitivity tests that fix strain rates to $5 \times 10^{-14} \text{ s}^{-1}$; this range in strain rate is derived using the range in velocity gradients determined in geodynamic models of the mantle wedge [e.g., Syracuse *et al.*, 2010]. These calculations indicate that dislocation creep is the dominant deformation mechanism in the mantle wedge for a wide range of conditions (i.e., at temperatures greater than $800\text{--}900^\circ\text{C}$, dislocation creep viscosities are lower than paleowattmeter diffusion creep viscosities). It is noteworthy that for the grain sizes predicted at arc and back-arc mantle temperatures, the dislocation creep viscosity is approximately 2–3 orders of magnitude lower than that predicted for diffusion creep—highlighting the extremely strong grain size dependence of diffusion creep (viscosity scales as d^3). Similar calculations and forward models have been used previously to argue that dislocation creep is the likely cause of

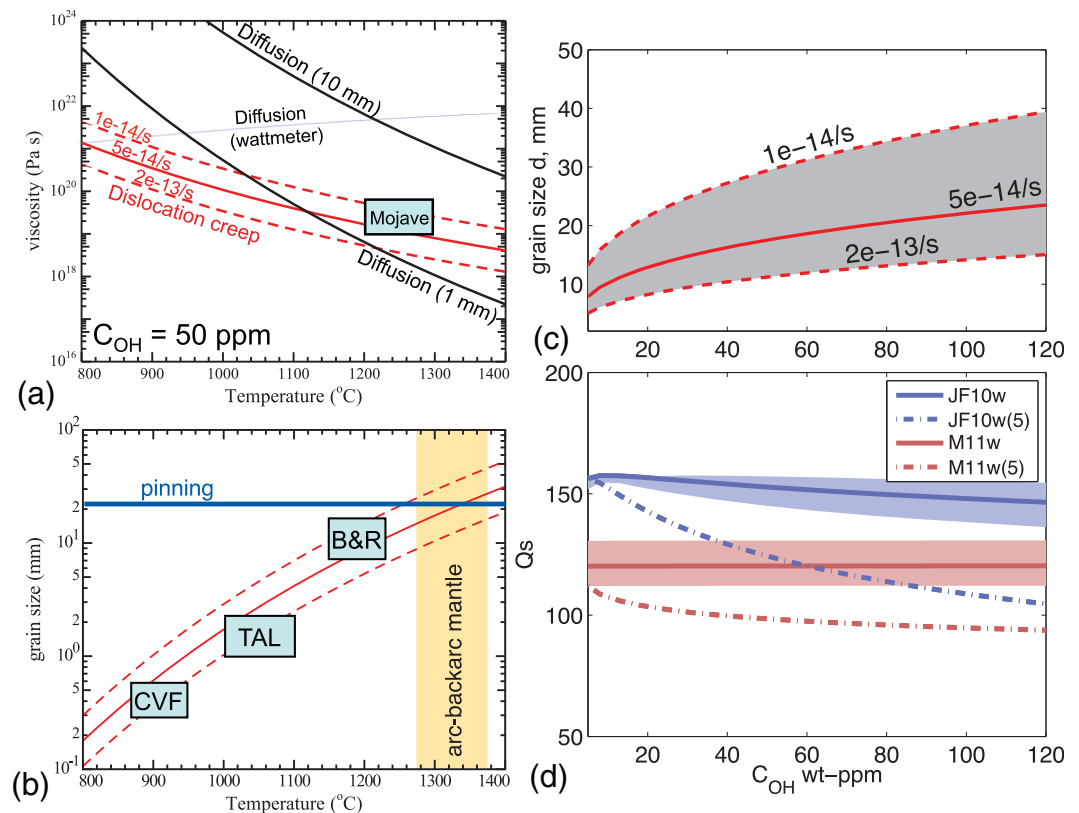


Figure 8. Effective viscosity (η) and grain size (d) in damp peridotite. (a) η versus T for diffusion creep, at $d = 1$ and 10 mm and dislocation creep at three different strain rates (labeled), for 50 wt ppm water, in damp olivine [Hirth and Kohlstedt, 2003] recalibrated for OH [Bell et al., 2003]. A η estimate based on analyses of postseismic creep data from the Mojave Region of the Western U.S. [Freed et al., 2012] is also shown. (b) d predicted for olivine with 50 wt ppm water, for the same three strain rates (red lines), predicted using the wattmeter relationship [Austin and Evans, 2007; Behn et al., 2009]. Also shown are grain size data and temperature estimates for the Cima Volcanic Field (CVF) [Behr and Hirth, 2014]; the mantle section of the Talkeetna arc (TAL) [Mehl et al., 2003]; and the Basin and Range (B&R) [Avé Lallemant et al., 1980]. Horizontal line shows a potential limit in d due to pinning from secondary phases [Evans et al., 2001]. The estimate of diffusion creep viscosity based on the wattmeter is illustrated by the dotted line in Figure 8a. (c) d variation predicted for varying C_{OH} at 1300 $^{\circ}\text{C}$, at same strain conditions. (d) Q_5 variations predicted at 1300 $^{\circ}\text{C}$, 2.5 GPa, and 1 Hz for C_{OH} , for modified versions of models M11w (M11 with Maxwell scaling to corrected wet diffusion creep law of Hirth and Kohlstedt [Hirth and Kohlstedt, 2003; Bell et al., 2003]) and JF10w (JF10 with relaxation times scaled to C_{OH} via equation (15)). Solid fields show range of Q_5 for the range of strain rates in Figures 8a-8c. Models M11w(5) and JF10w(5) incorporate same water weakening effects as M11w and JF10w, respectively, but fix d to 5 mm.

seismic anisotropy in the upper mantle for grain sizes in the range of several millimeters [e.g., Karato, 1992; Becker, 2006].

The grain sizes predicted for the mantle wedge using these flow laws and the parameterization outlined by Behn et al. [2009] are illustrated in Figure 8b. For these conditions, grain sizes of $\sim 500 \mu\text{m}$ –30 mm are predicted for damp mantle at 900–1400 $^{\circ}\text{C}$, corresponding well to xenoliths from the Cima Volcanic Zone [Behr and Hirth, 2014], the Basin and Range [Mercier, 1980], and the exhumed mantle section of the Talkeetna Arc [Mehl et al., 2003]. The relatively large grain size predicted for the hottest, low-viscosity region of the mantle wedge is also similar to that predicted for the convecting mantle wedge using the same approach used here [Wada et al., 2011]. In general, any estimate of strain and stresses over the hot flowing part of the mantle wedge, where the Q_5 measurements are made, results in grain sizes of a few mm to cm, consistent with direct observations and other estimations as described above.

The largest grain sizes calculated at high temperatures, $\gg 10$ mm, may overestimate grain size owing to the effects of pinning from secondary phases (e.g., garnet and pyroxene). Models for second-phase pinning, in which olivine grain size is limited by pinning and the size of the pinning phases are in turn limited by relatively sluggish Ostwald ripening, indicate grain sizes on order of 10–30 mm may be stabilized over periods of ~ 100 Ma [Evans et al., 2001].

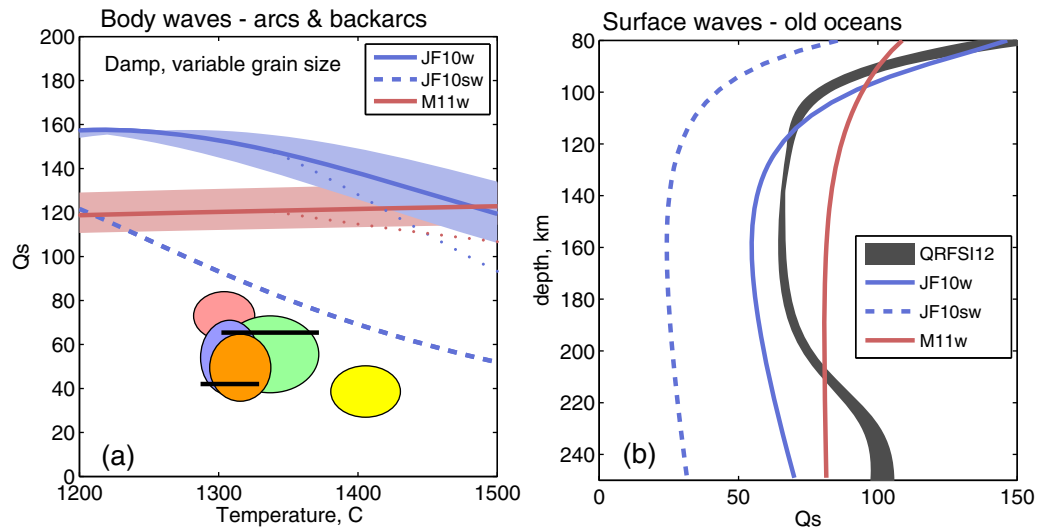


Figure 9. Q_5 observations and predictions for damp olivine and temperature-dependent d . (a) Body wave Q_5 and T measurements (ovals and bars) as described in Figure 7. The d estimates are calculated for nominal strain rates of $5E-14/s$ (solid lines), or ranging between $1E-14/s$ and $2E-13/s$ (shaded fields) as Figure 8. Dotted lines show effect of “pinned” pins grain sizes assuming 10 mm opx crystals. All calculations at $f = 1$ Hz, $P = 2.5$ GPa, and $C_{OH} = 50$ wt ppm. (b) Surface-wave attenuation model QRFSI12/ref1 for 100–160 Ma Pacific mantle (gray field) [Dalton *et al.*, 2009], compared with predictions. In these predictions, d increases linearly reaching 11 and 15 mm at 150 and 400 km depth as estimated for old lithosphere and $C_{OH} = 1000$ ppm H/Si [Behn *et al.*, 2009]. Temperatures follow half-space cooling for 100 Ma lithosphere with thermal diffusivity of $8.04E-5$ $m^2 s^{-1}$ [Stein and Stein, 1992], reaching a potential temperature of $1350^\circ C$ and increasing adiabatically (0.3 $K km^{-1}$). Dominant frequency of predictions (Hz) increase with depth Z (m) as $f = (4200 m s^{-1})/(3Z)$ following Forsyth [1992]. In both figures, models JF10w and JF10sw are as modified from Figure 7’s JF10 and JF10s, respectively, by varying grain size as in Figure 8 and adding water weakening scaling relaxation times by equation (15); M11w is similar to M11 but with variable grain size as Figure 8 and wet diffusion viscosity of Hirth and Kohlstedt [2003].

5.3. Effects of H₂O

Although direct experimental evidence for the effect of H₂O on attenuation is scant, it is possibly significant [Karato, 2003; Aizawa *et al.*, 2008]. Water affects attenuation in at least two ways. First, it promotes viscous and viscoelastic relaxation. We can estimate this effect on attenuation by scaling to laboratory-calibrated reductions in viscosity η (or relaxation times $\tau = \eta/G_U$) from its dry value η_{dry} [Karato, 2003], e.g.,

$$\eta = \eta_{dry} (C_{OH}/C_{OH-R})^{-r}, \quad (15)$$

where C_{OH} is the water concentration, C_{OH-R} is a nominal C_{OH} below which the viscous response is nominally unaffected by the presence of dissolved hydrogen and r is an appropriate exponent. Olivine flow laws show $C_{OH-R} = 50$ ppm H/Si (~ 3 wt ppm) corresponds to the transition from wet to dry behavior, and $r = 1.0$ for diffusion creep [Mei and Kohlstedt, 2000; Hirth and Kohlstedt, 2003]. For the attenuation relations of JF10, we incorporate water effects by scaling all anelastic and viscous relaxation times by $(C_{OH}/C_{OH-R})^{-r}$. Thus, the scaling applied here assumes that all viscosities and viscoelastic relaxation times obey similar weakening trends [e.g., Olugboji *et al.*, 2013]. For attenuation relations that depend explicitly on Maxwell-frequency scaling (M11), we directly apply viscosities from the damp diffusion creep flow law of Hirth and Kohlstedt [2003], increased by a factor of 3 to account for OH recalibration [Bell *et al.*, 2003].

A second, competing effect is that increasing C_{OH} will also lead to larger grain sizes. Increasing grain size acts to decrease attenuation, by an amount comparable to the direct weakening of hydrogen for the temperatures considered here. This trade-off is illustrated in Figure 8d, which shows that grain size increases with C_{OH} so that Q_5 remains roughly constant. This trade-off would be mitigated if grain size were pinned by second phases.

In any case, Figure 9a illustrates that the low Q_5 in arcs and back arcs is difficult to explain by including the influence of water in the scaling relations of JF10 and M11; corresponding models are termed JF10w and M11w. In fact, the lowest Q_5 values occur beneath back-arc spreading centers not volcanic arcs, where H₂O contents are expected to be several times lower [Kelley *et al.*, 2010], so variations in Q_5 seem to be the opposite of what any H₂O effect should produce [Pozgay *et al.*, 2009]. The JF10sw model, derived from the sol-

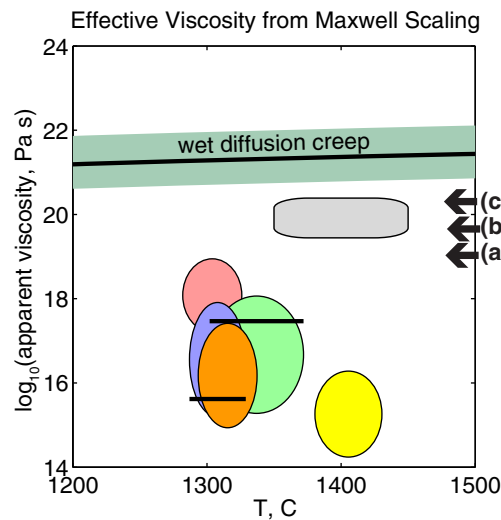


Figure 10. Viscosities estimated from Q_5 assuming Maxwell-frequency scaling (M11). Ovals show same arc and back-arc data as Figure 7, converting Q_5 to viscosity via M11. Gray field shows estimate from beneath 100–160 Ma lithosphere from surface waves [Dalton et al., 2009] and corresponding asthenospheric temperature estimates (Figure 9). Solid line and green field show predictions for wet grain-boundary diffusion creep at wattmeter-derived grain sizes for same range of strain rates as Figure 8. Arrows on the right show some potentially relevant estimates of viscosity: (a) steady state postseismic relaxation in subduction zones [summarized in Burgmann and Dresen, 2008]; (b) East California Shear Zone mantle [Freed et al., 2012]; (c) glacial isostatic adjustment [Milne et al., 2001; Tamisea et al., 2007]. Although the surface-wave estimate beneath the old Pacific is broadly consistent with other constraints, the arc data lie orders of magnitude lower, indicating a breakdown in Maxwell scaling.

both of these data sets. Attenuation in one of these geodynamic settings is probably influenced by other phenomena, the most likely candidate being the effect of in situ melt on the arc/back-arc environment. It is also possible that these discrepancies reflect some aspect of frequency dependence (i.e., a frequency dependence smaller than that currently constrained by laboratory studies) that is not yet understood, since the two seismological data sets are constrained at roughly 2 orders of magnitude different frequency.

5.4. Maxwell Viscosity Scaling

The Maxwell-frequency scaling of M11 (where the reference time scale is defined by diffusion creep) applies to conditions in which the mechanism of attenuation is rate limited by diffusive transport along grain boundaries. If the attenuation data from our study had been perfectly predicted by the Maxwell-frequency scaling, similitude would dictate that the mechanism of attenuation was solely that of diffusionally accommodated grain-boundary sliding. In other words, if the Maxwell-frequency scaling of M11 is applicable then the steady state viscosity η_{ss} calculated by inverting equation (11) for a given measurement of Q should provide a good fit to independent estimates of mantle viscosity [e.g., Priestley and McKenzie, 2013]. Most geodetic estimates for uppermantle viscosity lie in the range of 10^{19} – 10^{21} Pa s [e.g., Burgmann and Dresen, 2008]. For example, analyses of postseismic creep data from the Mojave region [Freed et al., 2012] indicate steady state viscosities in the dislocation creep regime of $\sim 5 \times 10^{19}$ Pa s at 1250–1300°C (Figure 8a). As shown in Figure 10, the geodetic estimates are also broadly consistent with the viscosity inferred from attenuation data for surface waves at 110–200 km depth beneath the >100 Ma Pacific [Dalton et al., 2008]; these values are in turn approximately 1–2 orders of magnitude lower than that predicted by the damp grain-boundary diffusion law [Hirth and Kohlstedt, 2003] used for scaling model M11w (Figures 9a and 10). In contrast, using observed attenuation to constrain viscosity with the Maxwell-frequency scaling predicts low apparent viscosities beneath arcs and back arcs ranging from 10^{15} to 10^{18} Pa s, significantly below the geodetic constraints (although 10^{18} Pa s is within uncertainty of that required to model topography and the geoid above the mantle wedge [e.g., Billen and Gurnis, 2001]). Thus, rather than assuming exotic viscosities not otherwise observed, it is likely that the Maxwell scaling breaks down at conditions of

gel-only fit of JF10, provides the closest match to the observed Q_5 owing to the modestly lower grain size dependence that results in a smaller increase in Q_5 for the extrapolation from laboratory to natural conditions.

In contrast, surface-wave observations from old oceans [Dalton et al., 2008, 2009] are similar to predictions for damp, equilibrium-grain size olivine-dominated rocks for most of these models (Figure 9b). The correspondence is fairly strong; models JF10w and M11w both predict Q_5 to within 20% of observations over much of the asthenospheric depth ranges. The one exception here is model JF10sw which underpredicts surface-wave Q_5 by a factor of 2 at least; this model is closest to the body wave data. Thus, the same damp viscosity/attenuation model cannot fit

the subarc mantle. Such a scaling breakdown is suggested by recent observations of high-frequency absorption peaks in the lab, attributable to elastically accommodated grain-boundary sliding [Jackson *et al.*, 2014], enhanced attenuation owing to the presence of dislocations [Farla *et al.*, 2012], or to some other yet uncharacterized process [Takei *et al.*, 2014]. The scaling breakdown may partly reflect the lower effective viscosity resulting from the dominance of dislocation creep as the dominant steady state creep mechanism at mantle conditions (Figure 8a), indicating a break in the M11 scaling relationship with increasing grain size.

5.5. Melt

The discrepancy between observed and predicted attenuation could be explained if melt plays an important role in Q in some settings. Beneath arcs and back-arc spreading centers, surface basaltic volcanism requires significant mantle melt production and some in situ interconnected melt porosity. The observation that Q_5 from surface waves beneath old ocean basins match laboratory-based predictions but Q_5 from arcs does not (Figure 9b versus 9a) supports the notion that low Q_5 beneath arcs arises from the presence of melt, since melt is likely to be far more abundant beneath active volcanic centers than old ocean basins. However, the effect of melt on attenuation remains poorly constrained, as discussed below.

In some experimental studies, a direct increase of the HTB with small melt fractions has been reported [Gribb and Cooper, 2000; McCarthy and Takei, 2011], whereas others have observed a shape change in the spectra attributed to a melt-enhanced absorption peak [Jackson *et al.*, 2004]. Thus, we consider that melt can affect Q via two broad classes of processes. First, melt can directly increase the HTB dissipation, perhaps through Maxwell scaling to viscosity. We will consider several quantitative approaches that have been proposed in evaluating this effect. Second, we will consider how melt affects various absorption peaks on top of the HTB. However, experiments as of yet cannot scale these effects to mantle conditions, so we can only qualitatively evaluate this possibility.

5.5.1. Effects of Melt on the HTB

It is known that melt can reduce η_{ss} ; however, the magnitude of this reduction is not clear. In studies where the reference sample is considered genuinely melt free [e.g., Faul and Jackson, 2007; McCarthy and Takei, 2011], a viscosity drop of more than an order of magnitude has been observed with just a “whiff” of melt ($\ll 1\%$). In McCarthy and Takei [2011], the onset of melting also resulted in a significant increase in the HTB. When scaled using the η_{ss} , the attenuation measured for melt-bearing experimental samples fell on the same master curve as defined by melt-free samples, indicating that the HTB process was well predicted by Maxwell-frequency scaling. Theoretical treatment of the grain-boundary diffusion process indicates that the initial whiff of melt dramatically reduces the steady state viscosity as soon as the smallest tubules on triple junctions form, by greatly reducing diffusion distances [Takei and Holtzman, 2009]. Above this critical melt fraction ($\ll 1\%$ at mantle grain sizes), viscosity decreases more gradually [e.g., Hirth and Kohlstedt, 2003]. In the McCarthy and Takei [2011] experiments, very small melt fractions and melting-induced reductions in impurities reduced η_{ss} by 20–100 times in borneol (an organic salt). Faul and Jackson [2007] also indicate 1–2 orders of magnitude reduction in η_{ss} between genuinely melt-free and compositionally simple samples and those with $\ll 1\%$ melt. The Takei and Holtzman [2009] model predicts a very rapid drop in viscosity observed in these experiments but by a more modest factor of 5, providing theoretical justification for a smaller but strong melt whiff effect.

To evaluate these effects, we adjust the M11w and JF10w damp olivine attenuation models (Figure 9) by rescaling viscosity and relaxation times to account for melt (Figure 11). We adjust relaxation times in two ways: (1) a decrease of a factor of 5, consistent with contiguity theory [Takei and Holtzman, 2009], and (2) a much larger decrease at trace amounts of melt, nominally a factor of 42, to lie in the range of experiments [Faul and Jackson, 2007; McCarthy and Takei, 2011] to account for a variety of potential effects that are discussed below. The scaling of relaxation times and viscosity also includes a gradual reduction as melt fraction increases, of $\exp(-30\phi)$ as estimated by Hirth and Kohlstedt [2003]; ϕ is the in situ melt fraction. We reduce all relaxation times proportionately to creep, as with the H₂O corrections (section 5.3). The effect of water is still included because the H₂O estimates in olivine are based on equilibrium of peridotites with wet basaltic magmas, and we retain the grain size estimates described above.

Adding these melt effects to the M11w attenuation model does relatively little. At seismic frequencies, the M11 master curve has very little sensitivity to frequency so that the net effect on Q_5 is less than 25% this weak sensitivity explains why the viscosities predicted by the Maxwell-frequency scaling in Figure 10 are

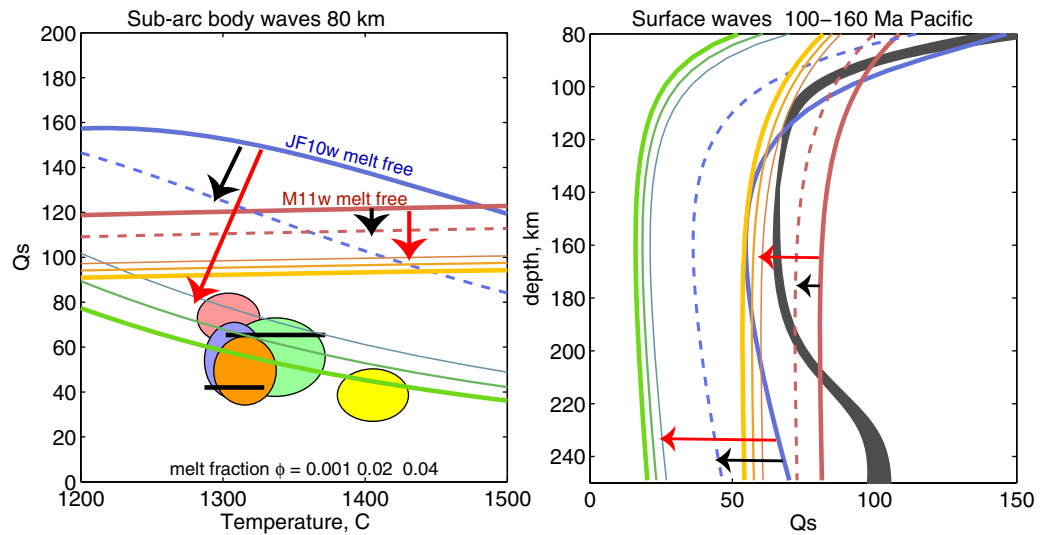


Figure 11. A range of melt effects compared with Q_5 observations. (a) Comparison with arc/back-arc data. Data were plotted with same symbols as Figure 7; calculations assume 1 Hz, 50 wt ppm H_2O , 2.5 GPa, strain rate of $5E-14/s$. (b) Comparison with surface-wave data for 100–160 Ma Pacific [Dalton *et al.*, 2008], calculations as in Figure 9. In both figures, Figure 9 describes data starting models M11w (red) and JF10w (blue). Models follow color scheme in Figure 7a. Dashed lines and black arrows: effect if melt gives a 5X reduction in all relaxation times and viscosity [Takei and Holtzman, 2009]; red arrows and remaining lines: larger 42X reduction in relaxation times at trace melt fractions accompanied by exponential weakening with increasing melt fraction [Hirth and Kohlstedt, 2003]. Green and yellow lines show with increasing line thickness melt fractions ϕ of 0.001, 0.02, and 0.04.

unrealistically low. By contrast, the JF10 model has greater dependence on frequency or relaxation times of $Q_5 \sim (\omega\tau_r)^2$ (i.e., the high-frequency dissipation peak is not encountered), so that these changes in relaxation time produce up to a factor of 5 reduction in Q_5 . The combination of the JF10 sensitivity to ω and the $\sim 42X$ viscosity drop can predict the high attenuation observed beneath both arcs and back arcs. We also investigated the melt model of Jackson *et al.* [2004], which predicts even lower Q_5 for $>1\%$ melt, but it lacks the corrections and consistent parameterization of JF10, and its fitting procedure overpredicts the effects of melt on Q (U. Faul, personal communication, 2013).

It remains unclear whether such large changes in viscosity with the onset of melting are applicable for mantle conditions. On one hand, the large viscosity drop associated with changes in impurity content may not be applicable for multiphase mantle peridotite. The abundance of most trace elements (e.g., REE) is extremely low in olivine, and the concentration other “impurity” components in olivine (such as Ca and Al, which may have important effects on grain-boundary properties [e.g., Hiraga *et al.*, 2004]) will not change significantly at the onset of melting, because these elements are compatible in coexisting phases (e.g., clinopyroxene). On the other hand, stress-driven melt segregation at length scales longer than the grain size has been shown to reduce the effective viscosity by up to an order of magnitude in experiments [Holtzman *et al.*, 2012]. If this process occurs in significant volumes of the mantle wedge, it is possible that the appropriate effective viscosity to use in the attenuation scaling is that of the effective medium at length scales much smaller than the seismic wavelength (but larger than the grain size), providing some justification for invoking a larger melt effect.

5.5.2. Melt-Induced Absorption Peaks

As indicated in section 5.4, the extremely low viscosities implied by arc and back-arc data imply that straightforward Maxwell-frequency scaling is violated. The presence of melt has been shown to increase attenuation above the background at seismic frequencies [e.g., Jackson *et al.*, 2004]. The melt effect has been attributed to either an enhancement of the elastically accommodated grain-boundary sliding or an additional melt-specific peak. The enhancement is proposed to be due to a decrease of grain-boundary viscosity [Sundberg and Cooper, 2010] and/or the rounding of grain edges at melt-filled triple junctions [Faul *et al.*, 2004; Jackson *et al.*, 2006; Barnhoorn *et al.*, 2007]. The presence of the dissipation peak has also been interpreted to result from a reduction in grain-boundary viscosity owing to the presence of pyroxene

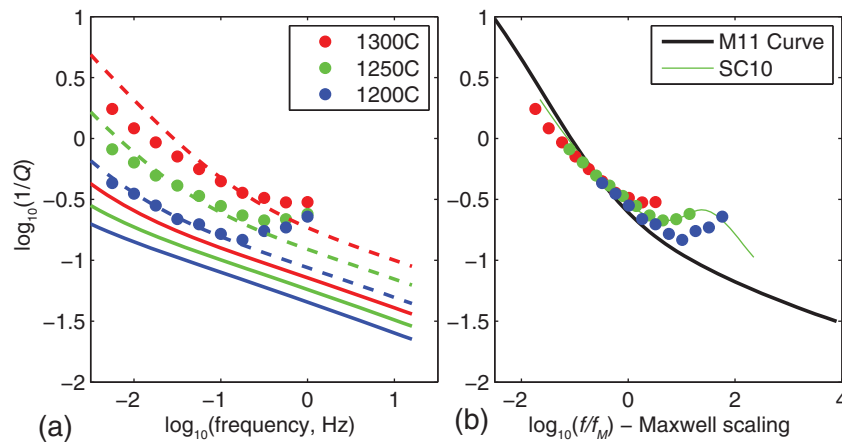


Figure 12. Comparison of peridotite attenuation data [Sundberg and Cooper, 2010] to models. Colors indicate temperature of experiments or prediction, as labeled. (a) Comparison to JF10. Solid lines show predictions at experimental conditions, dashed lines show predictions after adjusting all τ_i proportionately so that steady state creep rate matches that reported for the experiments. (b) Comparison to M11 master curve (thick line). For reference, thin green line shows the composite viscoelastic model including a Debye peak representing elastically accommodated grain-boundary sliding with $\Delta = 0.43$, for the 1250°C samples, assuming reported parameters for 1250°C data [Sundberg and Cooper, 2010]. While both M11 and the modified JF10 can explain low-frequency data, the clear peak shows $1/Q_5$ several times higher than predicted.

[Sundberg and Cooper, 2010], although Sundberg and Cooper’s experiments do not independently separate the effects of small melt fractions and the presence of pyroxene.

To illustrate the scaling breakdown, we compare the models of M11 and JF10 to the data of Sundberg and Cooper [2010] (Figure 12). Sundberg and Cooper’s experiments sample peridotites with 39% pyroxene content, at a single 5.2 μm grain size. Scaling their Q_5 with the directly measured η_{ss} shows good agreement with the M11 master curve at low frequencies, and if all the JF10 relaxation times are adjusted to match the observed steady state creep viscosity then the JF10 model predicts low-frequency behavior as well. However, at high frequencies, a clear dissipation peak is encountered which attenuates significantly more than predicted from either model, by a factor of 5 at least (the maximum of the peak is not encountered in these experiments).

Melt-specific attenuation mechanisms such as melt squirt [e.g., Mavko and Nur, 1975] may play a role. Melt squirt is generally assumed to operate at frequencies above those observed in the seismic band for the pore geometries observed in olivine-dominated rocks [Hammond and Humphreys, 2000; Faul et al., 2004], but it is possible that at the high body wave frequencies, nonequilibrium melt geometries and stress-driven melt segregation could make these effects more important [Cooper, 2002; Holtzman and Kendall, 2010]. A recent study showing thin (<100 nm) melt films in partially molten synthetic samples of olivine + basaltic melt [Garapic et al., 2013] have spurred a reinterpretation of dissipation peaks in previous studies of melt-bearing materials as being due to melt squirt between adjacent wetted grain boundaries with low aspect ratio [Jackson, 2014].

Unfortunately, the relevant experiments do not provide clear evidence of grain size and temperature scaling of the height, width and frequency of such peaks in melt-bearing rocks, making extrapolation of the few experiments showing melt effects to mantle conditions conjectural at best.

6. Conclusions

When compared systematically, regional body wave data sets show that the subarc mantle has high attenuation of Q_5 of 40–80, and back-arc spreading centers exhibit even lower Q_5 of 20–50. At all the sites observed, petrologically based geothermobarometers indicate temperatures of 1300–1450°C at the 80 km depths of maximum attenuation (minimum Q_5), in a manner that correlates with seismically based attenuation. These Q_5 values, corrected to 1 Hz, are 1.5–5 times below what is predicted by laboratory-based attenuation models for the Q_5 temperature dependence when extrapolated to mantle grain sizes. Laboratory-derived models such as JF10 and M11, although predicting similar dissipation at laboratory grain

sizes extrapolate to the mantle rather differently, but always to higher Q_5 values than observed in the sub-arc and back-arc mantle. Still, the correlation between seismic Q_5 measurements and petrologic temperature estimates indicates that attenuation has potential to quantitatively constrain mantle conditions.

We explore a suite of effects that may explain the difference (Figure 7a). Grain size evolution models provide a way to remove a degree of freedom in attenuation relations, by tying the equilibrium grain size to deformation rates and viscosity. Water weakens material and should reduce Q , but it increases grain sizes at the same time. For the scaling relations explored here, these two effects roughly cancel so that it is difficult to explain low Q_5 by water alone. Models with both effects included generally cannot explain the arc/back-arc data but do agree with Q_5 observed from surface waves beneath old ocean basins. It seems likely that the presence of melt beneath arcs and back arcs, necessary to produce observed volcanism, can sufficiently reduce Q_5 . The subarc Q_5 estimates appear to violate the Maxwell-frequency scaling that describes most laboratory measurements of high-temperature background attenuation, although some combination of models with sufficient frequency sensitivity in the seismic band can reproduce the seismic observations. It seems plausible that melt produces a high-temperature absorption peak or other enhanced mechanisms that attenuates seismic waves more than predicted by most laboratory-based melt-free models. However, the effect of melt on attenuation, particularly on potential dissipation peaks, remains poorly understood so that at present it is difficult to use attenuation to place quantitative constraints on melt abundance. Further progress on melt effects should be a high priority in laboratory-based attenuation studies.

Acknowledgments

This work supported by the National Science Foundation, grant EAR-1067974 (Lamont-Doherty), EAR-1067689 (Brown), and EAR-1067928 (Washington University). We thank S. Pozgay Rawlinson and K. Rychert for providing data files from their earlier studies, and S. Wei for results prior to publication. Stimulating discussions at a CIDER-sponsored workshop on mantle attenuation, May 2013, motivated and advanced this work, as did conversations with R. Cooper, C. Dalton, U. Faul, D. Forsyth, and Y. Takei. All data in this paper have been published previously and are available at open data centers (IRIS for seismic data, and as described in the supporting information for geochemistry).

References

- Aizawa, Y., A. Barnhoorn, U. H. Faul, J. D. FitzGerald, I. Jackson, and I. Kovacs (2008), Seismic properties of Anita Bay Dunite: An exploratory study of the influence of water, *J. Petrol.*, *49*(4), 841–854.
- Anderson, D. L., and J. W. Given (1982), Absorption band Q model for the Earth, *J. Geophys. Res.*, *87*, 3893–3904.
- Austin, N. J., and B. Evans (2007), Paleowattmeters: A scaling relation for dynamically recrystallized grain size, *Geology*, *35*(4), 343–346.
- Avé Lallemant, H., J. Mercier, N. Carter, and J. Ross (1980), Rheology of the upper mantle: Inferences from peridotite xenoliths, *Tectonophysics*, *70*, 85–113.
- Barnhoorn, A., I. Jackson, J. D. F. Gerald, and Y. Aizawa (2007), Suppression of elastically accommodated grain-boundary sliding in high-purity MgO, *J. Eur. Ceram. Soc.*, *27*, 4697–4703.
- Becker, T. W. (2006), On the effect of temperature and strain-rate dependent viscosity on global mantle flow, net rotation, and driving forces, *Geophys. J. Int.*, *167*, 943–957.
- Behn, M. D., G. Hirth, and J. R. Elsenbeck (2009), Implications of grain size evolution on the seismic structure of the oceanic upper mantle, *Earth Planet. Sci. Lett.*, *282*, 178–189.
- Behr, W. M., and G. Hirth (2014), Rheological properties of the mantle lid beneath the Mojave region in southern California, *Earth Planet. Sci. Lett.*, *383*, 60–72.
- Bell, D. R., G. R. Rossman, J. Maldener, D. Endisch, and F. Rauch (2003), Hydroxide in olivine: A quantitative determination of the absolute amount and calibration of the IR spectrum, *J. Geophys. Res.*, *108*(B2), 2105, doi:10.1029/2001JB000679.
- Berckhemer, H., W. Kampfmann, E. Aulbach, and H. Schmeling (1982), Shear modulus and Q of fosterite and dunite near partial melting from forced-oscillation experiments, *Phys. Earth Planet. Inter.*, *29*, 30–41.
- Billen, M. I., and M. Gurnis (2001), A low viscosity wedge in subduction zones, *Earth Planet. Sci. Lett.*, *193*, 227–236.
- Booth, C. M., D. W. Forsyth, and D. S. Weeraratne (2014), Upper mantle Q structure beneath old seafloor in the western Pacific, *J. Geophys. Res. Solid Earth*, *119*, 3448–3461, doi:10.1002/2013JB010589.
- Burgmann, R., and G. Dresen (2008), Rheology of the lower crust and upper mantle: Evidence from rock mechanics, geodesy, and field observations, *Annu. Rev. Earth Planet. Sci.*, *36*, 531–567.
- Cooper, R. F. (2002), Seismic wave attenuation: Energy dissipation in viscoelastic crystalline solids, *Rev. Mineral. Geochem.*, *51*, 253–290.
- Dalton, C. A., G. Ekström, and A. M. Dziewonski (2008), The global attenuation structure of the upper mantle, *J. Geophys. Res.*, *113*, B09303, doi:10.1029/2007JB005429.
- Dalton, C. A., G. Ekström, and A. M. Dziewonski (2009), Global seismological shear velocity and attenuation: A comparison with experimental observations, *Earth Planet. Sci. Lett.*, *284*, 65–75.
- Dziewonski, A. M., and D. L. Anderson (1981), Preliminary reference Earth model, *Phys. Earth Planet. Inter.*, *25*, 297–356.
- Eberhart-Phillips, D., M. Chadwick, and S. Bannister (2008), Three-dimensional attenuation structure of central and southern South Island, New Zealand, from local earthquakes, *J. Geophys. Res.*, *113*, B05308, doi:10.1029/2007JB005359.
- Elkins-Tanton, L. G., T. L. Grove, and J. Donnelly-Nolan (2001), Hot shallow mantle melting under the Cascades volcanic arc, *Geology*, *29*, 631–634.
- Evans, B., J. Renner, and G. Hirth (2001), A few remarks on the kinetics of grain growth in rocks, *Int. J. Earth Sci.*, *90*, 88–103.
- Farla, R. J. M., I. Jackson, J. D. FitzGerald, U. H. Faul, and M. E. Zimmerman (2012), Dislocation damping and anisotropic seismic wave attenuation in Earth's upper mantle, *Science*, *336*, 332–335.
- Faul, U. H., and I. Jackson (2007), Diffusion creep of dry, melt-free olivine, *J. Geophys. Res.*, *112*, B04204, doi:10.1029/2006JB004586.
- Faul, U. H., J. D. FitzGerald, and I. Jackson (2004), Shear wave attenuation and dispersion in melt-bearing olivine polycrystals: 2. Microstructural interpretation and seismological implications, *J. Geophys. Res.*, *109*, B06202, doi:10.1029/2003JB002407.
- Forsyth, D. W. (1992), Geophysical constraints on mantle flow and melt generation beneath mid-ocean ridges, in *Mantle Flow and Melt Generation at Mid-Ocean Ridges*, *Geophys. Monogr. Ser.*, vol. 71, edited by J. Phipps-Morgan et al., pp. 1–66, AGU, Washington, D. C.
- Freed, A. M., G. Hirth, and M. D. Behn (2012), Using short-term postseismic displacements to infer the ambient deformation conditions of the upper mantle, *J. Geophys. Res.*, *117*, B01409, doi:10.1029/2011JB008562.

- Gaetani, G. A., J. A. O'Leary, N. Shimizu, C. E. Bucholz, and M. Newville (2012), Rapid re-equilibration of H₂O and oxygen fugacity in olivine-hosted inclusions, *Geology*, *40*, 915–918, doi:10.1130/G32992.1.
- Garapčić, G., U. Faul, and E. Brisson (2013), High-resolution imaging of the melt distribution in partially molten upper mantle rocks: Evidence for wetted two-grain boundaries, *Geochem. Geophys. Geosyst.*, *14*, 556–566, doi:10.1029/2012GC004547.
- Gazel, E., T. Plank, D. Forsyth, C. Bendersky, C.-T. A. Lee, and E. H. Hauri (2012), Lithosphere vs. asthenosphere sources at Big Pine Volcanic field, *Geochem. Geophys. Geosyst.*, *13*, Q0AK06, doi:10.1029/2012GC004060.
- Gribb, T. T., and R. F. Cooper (1998), Low-frequency shear attenuation in polycrystalline olivine: Grain boundary diffusion and the physical significance of the Andrade model for viscoelastic rheology, *J. Geophys. Res.*, *103*, 27,267–27,279.
- Gribb, T. T., and R. F. Cooper (2000), The effect of an equilibrated melt phase on the shear creep and attenuation behavior of polycrystalline olivine, *Geophys. Res. Lett.*, *27*, 2341–2344.
- Hammond, W. C., and E. D. Humphreys (2000), Upper mantle seismic wave attenuation: Effects of realistic partial melt distribution, *J. Geophys. Res.*, *105*, 10,987–10,999.
- Hauri, E. H., G. A. Gaetani, and T. H. Green (2006), Partitioning of water during melting of the Earth's upper mantle at H₂O-undersaturated conditions, *Earth Planet. Sci. Lett.*, *248*, 715–734.
- Hiraga, T., I. M. Anderson, and D. L. Kohlstedt (2004), Grain boundaries as reservoirs of incompatible elements in the Earth's mantle, *Nature*, *427*, 699–703.
- Hirschmann, M. M. (2000), Mantle solidus: Experimental constraints and the effects of peridotite composition, *Geochem. Geophys. Geosyst.*, *1*(10), 1042, doi:10.1029/2000GC000070.
- Hirschmann, M. M., T. Tenner, C. Aubaud, and A. C. Withers (2009), Dehydration melting of nominally anhydrous mantle: the primacy of partitioning, *Phys. Earth Planet. Int.*, *176*, 54–68.
- Hirth, G., and D. Kohlstedt (2003), Rheology of the upper mantle and mantle wedge: A view from the experimentalists, in *Inside the Subduction Factory*, *Geophys. Monogr. Ser.*, vol. 138, edited by J. M. Eiler, pp. 83–106, AGU, Washington, D. C.
- Holtzman, B. K., and J.-M. Kendall (2010), Organized melt, seismic anisotropy, and plate boundary lubrication, *Geochem. Geophys. Geosyst.*, *11*, Q0AB06, doi:10.1029/2010GC003296.
- Holtzman, B. K., D. S. H. King, and D. L. Kohlstedt (2012), Effects of stress-driven melt segregation on the viscosity of rocks, *Earth Planet. Sci. Lett.*, *359–360*, 184–193.
- Jackson, D. D., and D. L. Anderson (1970), Physical mechanisms of seismic-wave attenuation, *Rev. Geophys.*, *8*, 1–63.
- Jackson, I. (2014), Properties of rocks and minerals—Physical origins of anelasticity & attenuation in rock, in *Treatise on Geophysics*, 2nd ed., edited by G. Schubert, Elsevier, Amsterdam, in press.
- Jackson, I., and U. H. Faul (2010), Grain-size-sensitive viscoelastic relaxation in olivine: Toward a robust laboratory-based model for seismological application, *Phys. Earth Planet. Inter.*, *183*, 151–163.
- Jackson, I., J. D. FitzGerald, U. H. Faul, and B. H. Tan (2002), Grain-size-sensitive seismic wave attenuation in polycrystalline olivine, *J. Geophys. Res.*, *107*(B12), 2360, doi:10.1029/2001JB001225.
- Jackson, I., U. H. Faul, J. D. FitzGerald, and B. H. Tan (2004), Shear wave attenuation and dispersion in melt-bearing olivine polycrystals: 1. Specimen fabrication and mechanical testing, *J. Geophys. Res.*, *109*, B06201, doi:10.1029/2003JB002406.
- Jackson, I., U. H. Faul, J. D. FitzGerald, and S. J. S. Morris (2006), Contrasting viscoelastic behaviour of melt-free and melt-bearing olivine: Implications for the nature of grain-boundary sliding, *Mater. Sci. Eng. A*, *442*, 170–174.
- Jackson, I., U. H. Faul, and R. Skelton (2014), Elastically accommodated grain-boundary sliding: New insights from experiment and modeling, *Phys. Earth Planet. Inter.*, *228*, 203–210.
- Karato, S. (1992), On the Lehmann discontinuity, *Geophys. Res. Lett.*, *19*, 2255–2258.
- Karato, S. (1993), Importance of anelasticity in the interpretation of seismic tomography, *Geophys. Res. Lett.*, *20*, 1623–1626.
- Karato, S. (2003), Mapping water content in the upper mantle, in *Inside the Subduction Factory*, *Geophys. Monogr. Ser.*, vol. 138, edited by J. M. Eiler, pp. 135–152, AGU, Washington, D. C.
- Karato, S., and H. A. Spetzler (1990), Defect microdynamics in minerals and solid-state mechanisms of seismic wave attenuation and velocity dispersion in the mantle, *Rev. Geophys.*, *28*, 399–421.
- Kelley, K. A., T. Plank, S. Newman, E. M. Stolper, T. L. Grove, S. Parman, and E. H. Hauri (2010), Mantle melting as a function of water content beneath the Mariana Arc, *J. Petrol.*, *51*(8), 1711–1738.
- Knopoff, L. (1964), *Q*, *Rev. Geophys.*, *2*, 625–660.
- Langmuir, C. H., and G. N. Hanson (1981), Calculating mineral-melt equilibria with stoichiometry, mass balance, and single component distribution coefficients, in *Thermo-Dynamics of Minerals and Melts*, edited by R. C. Newton, A. Navrotsky, and B. J. Wood, pp. 247–271, Springer, N. Y.
- Langmuir, C. H., E. M. Klein, and T. Plank (1992), Petrological systematics of mid-ocean ridge basalts: Constraints on melt generation beneath ocean ridges, in *Mantle Flow and Melt Generation at Mid-Ocean Ridges*, *Geophys. Monogr. Ser.*, vol. 71, edited by J. Phipps-Morgan et al., pp. 183–280, AGU, Washington, D. C.
- Lee, C.-T. A., P. Luffi, T. Plank, H. Dalton, and W. P. Leeman (2009), Constraints on the depths and temperatures of basaltic magma generation on Earth and other terrestrial planets using new thermobarometers for mafic magmas, *Earth Planet. Sci. Lett.*, *279*, 20–33.
- Lekic, V., J. Matas, M. Panning, and B. Romanowicz (2009), Measurement and implications of frequency dependence of attenuation, *Earth Planet. Sci. Lett.*, *282*, 285–293.
- Liang, X., E. Sandvol, S. Kay, B. Heit, X. Yuan, P. Mulcahy, C. Chen, L. Brown, D. Comte, and P. Alvarado (2014), Delamination of southern Puna lithosphere revealed by body wave attenuation tomography, *J. Geophys. Res. Solid Earth*, *119*, 549–566, doi:10.1002/2013JB010309.
- Mavko, G. M., and A. Nur (1979), Wave attenuation in partially saturated rocks, *Geophysics*, *44*, 161–178.
- McCarthy, C., and Y. Takei (2011), Anelasticity and viscosity of partially molten rock analogue: Toward seismic detection of small quantities of melt, *Geophys. Res. Lett.*, *38*, L18306, doi:10.1029/2011GL048776.
- McCarthy, C., Y. Takei, and T. Hiraga (2011), Experimental study of attenuation and dispersion over a broad frequency range: 2. The universal scaling of polycrystalline materials, *J. Geophys. Res.*, *116*, B09207, doi:10.1029/2011JB008384.
- Mehl, L., B. R. Hacker, G. Hirth, and P. B. Kelemen (2003), Arc-parallel flow within the mantle wedge: Evidence from the accreted Talkeetna arc, south central Alaska, *J. Geophys. Res.*, *108*(B8), 2375, doi:10.1029/2002JB002233.
- Mei, S., and D. L. Kohlstedt (2000), Influence of water on deformation of olivine aggregates: 1. Diffusion creep regime, *J. Geophys. Res.*, *105*, 21,457–21,469.
- Mercier, J.-C. C. (1980), Magnitude of the continental lithospheric stresses inferred from rheomorphic petrology, *J. Geophys. Res.*, *85*, 6293–6303.

- Milne, G. A., J. L. Davis, J. X. Mitrovica, H.-G. Scherneck, J. M. Johansson, M. Vermeer, and H. Koivula (2001), Space-geodetic constrains on glacial isostatic adjustment in Fennoscandia, *Science*, *291*, 2381–2385.
- Morris, S. J. S., and I. Jackson (2009), Implications of the similarity principle relating creep and attenuation in finely grained solids, *Mater. Sci. Eng. A*, *521–22*, 124–127.
- Nakajima, J., S. Hada, E. Hayami, N. Uchida, A. Hasegawa, S. Yoshioka, T. Matsuzawa, and N. Umino (2013), Seismic attenuation beneath northeastern Japan: Constraints on mantle dynamics and arc magmatism, *J. Geophys. Res.*, *118*, 5838–5855, doi:10.1002/2013JB010388.
- Nowick, A. S., and B. S. Berry (1972), *Anelastic Relaxation in Crystalline Solids*, 677 p., Academic, N. Y.
- Olugboji, T. M., S. Karato, and J. Park (2013), Structures of the oceanic lithosphere-asthenosphere boundary: Mineral-physics modeling and seismological signatures, *Geochem. Geophys. Geosyst.*, *14*, 880–901, doi:10.1002/ggge.20086.
- Plank, T., K. A. Kelley, M. M. Zimmer, E. H. Hauri, and P. J. Wallace (2013), Why do mafic arc magmas contain ~4 wt% water on average? *Earth Planet. Sci. Lett.*, *364*, 168–179.
- Pozgay, S. H., D. A. Wiens, J. A. Conder, H. Shiobara, and H. Sugioka (2009), Seismic attenuation tomography of the Mariana subduction system: Implications for thermal structure, volatile distribution, and slow spreading dynamics, *Geochem. Geophys. Geosyst.*, *10*, Q04X05, doi:10.1029/2008GC002313.
- Priestley, K., and D. McKenzie (2013), The relationship between shear wave velocity, temperature, attenuation and viscosity in the shallow part of the mantle, *Earth Planet. Sci. Lett.*, *381*, 78–91.
- Raj, R., and M. F. Ashby (1971), On grain boundary sliding and diffusional creep, *Metall. Trans. A*, *2*, 1113–1127.
- Roeder, P. L., and R. F. Emslie (1970), Olivine-liquid equilibrium, *Contrib. Mineral. Petrol.*, *29*, 275–289.
- Roth, E. G., D. A. Wiens, L. M. Dorman, J. Hildebrand, and S. C. Webb (1999), Seismic attenuation tomography of the Tonga back-arc region using phase pair methods, *J. Geophys. Res.*, *104*, 4795–4809.
- Rychert, C. A., K. M. Fischer, G. A. Abers, T. Plank, E. Syracuse, J. M. Protti, V. Gonzalez, and W. Strauch (2008), Strong along-arc variations in attenuation in the mantle wedge beneath Costa Rica and Nicaragua, *Geochem. Geophys. Geosyst.*, *9*, Q10S10, doi:10.1029/2008GC002040.
- Schurr, B., G. Asch, A. Rietbrock, R. Trumbull, and C. Haberland (2003), Complex patterns of fluid and melt transport in the central Andean subduction zone revealed by attenuation tomography, *Earth Planet. Sci. Lett.*, *215*, 105–119.
- Shito, A., S. Karato, K. N. Matsukage, and Y. Nishihara (2006), Toward mapping the three-dimensional distribution of water in the upper mantle from velocity and attenuation tomography, in *Earth's Deep Water Cycle*, *Geophys. Monogr.*, *168*, edited by S. D. Jacobsen and S. van der Lee, pp. 225–236, *Amer. Geophys. Un.*, Washington, D. C.
- Sipkin, S. A., and T. H. Jordan (1979), Frequency dependence of QScS, *Bull. Seismol. Soc. Am.*, *69*, 1055–1079.
- Stachnik, J. C., G. A. Abers, and D. Christensen (2004), Seismic attenuation and mantle wedge temperatures in the Alaska subduction zone, *J. Geophys. Res.*, *109*, B10304, doi:10.1029/2004JB003018.
- Stein, C. A., and S. Stein (1992), A model for the global variation in oceanic depth and heat flow with lithospheric age, *Nature*, *359*, 123–129.
- Sundberg, M., and R. F. Cooper (2010), A composite viscoelastic model for incorporating grain boundary sliding and transient diffusion creep; correlating creep and attenuation responses for materials with a fine grain size, *Philos. Mag.*, *90*(20), 2817–2840.
- Syracuse, E. M., P. E. van Keken, and G. A. Abers (2010), The global range of subduction zone thermal models, *Phys. Earth Planet. Inter.*, *183*, 73–90, doi:10.1016/j.pepi.2010.1002.1004.
- Takei, Y., and B. K. Holtzman (2009), Viscous constitutive relations of solid-liquid composites in terms of grain boundary contiguity: 2. Compositional model for small melt fractions, *J. Geophys. Res.*, *114*, B06206, doi:10.1029/2008JB005851.
- Takei, Y., F. Karasawa, and H. Yamauchi (2014), Temperature, grain size, and chemical controls on polycrystal anelasticity over a broad frequency range extending into the seismic range, *J. Geophys. Res.*, *119*, 5414–5443, doi:10.1002/2014JB011146.
- Tamisea, M. E., J. X. Mitrovica, and J. L. Davis (2007), GRACE gravity data constrain ancient ice geometries and continental dynamics over Laurentia, *Science*, *316*, 881–883.
- Tatsumi, Y., M. Sakuyama, H. Fukuyama, and I. Kushiro (1983), Generation of arc basalt magmas and thermal structure of the mantle wedge in subduction zones, *J. Geophys. Res.*, *88*, 5815–5825.
- Wada, I., M. D. Behn, and J. He (2011), Grain-size distribution in the mantle wedge of subduction zones, *J. Geophys. Res.*, *116*, B10203, doi:10.1029/2011JB008294.
- Wei, S. S., H. N. Relyea, D. A. Wiens, S. C. Webb, D. K. Blackman, R. A. Dunn, and J. A. Conder (2013), 3-D distribution of partial melt beneath the Lau Backarc Basin from seismic attenuation tomography, Abstract D123B-07 presented at 2013 Fall Meeting, AGU, San Francisco, Calif.
- Wiens, D. A., J. A. Conder, and U. H. Faul (2008), The seismic structure and dynamics of the mantle wedge, *Annu. Rev. Earth Planet. Sci.*, *36*, 421–455.
- Wiens, D. A., K. A. Kelley, and T. Plank (2006), Mantle temperature variations beneath back-arc spreading centers inferred from seismology, petrology and bathymetry, *Earth Planet. Sci. Lett.*, *248*, 30–42.
- Xu, Y., M. E. Zimmerman, and D. L. Kohlstedt (2002), Deformation behavior of partially molten mantle rocks, in *Rheology and Deformation of the Lithosphere at Continental Margins*, edited by G. D. Karner et al., pp. 284–310, Columbia Univ., New York, N. Y.